Unusual Electron Correlations in Na_xCoO_2 Due to the Spin-State Quasidegeneracy of Cobalt Ions

Jiří CHALOUPKA[1,2] and Giniyat KHALIULLIN[1]

[1] *Max-Planck-Institut für Festkörperforschung, Heisenbergstrasse 1, D-70569 Stuttgart, Germany*
[2] *Department of Condensed Matter Physics, Faculty of Science, Masaryk University, Kotlářská 2, 61137 Brno, Czech Republic*

Recent studies exposed many remarkable properties of layered cobaltates Na_xCoO_2. Surprisingly, many-body effects have been found to increase at sodium-rich compositions of Na_xCoO_2 where one expects a simple, nearly free motion of the dilute $S = 1/2$ holes doped into a band insulator $NaCoO_2$. Here we discuss the origin of enigmatic correlations that turn a doped $NaCoO_2$ into a strongly correlated electronic system. A minimal model including orbital degeneracy is proposed and its predictions are discussed. The model is based on a key property of cobalt oxides — the spin-state quasidegeneracy of CoO_6 octahedral complex — which has been known, e.g., in the context of an unusual physics of $LaCoO_3$ compound. Another important ingredient of the model is the 90° Co-O-Co bonding in Na_xCoO_2 which allows nearest-neighbor t_{2g}-e_g hopping. This hopping introduces a dynamical mixture of electronic configurations $t_{2g}^6, S = 0$ and $t_{2g}^5 e_g^1, S = 1$ of neighboring cobalt ions. We show that scattering of charge carriers on spin-state fluctuations suppresses their coherent motion and leads to the spin-polaron physics at $x \sim 1$. At larger doping when coherent fermionic bands are formed, the model predicts singlet superconductivity of extended s-wave symmetry. The presence of low-lying spin states of Co^{3+} is essential for the pairing mechanism. Implications of the model for magnetic orderings are also discussed.

§1. Introduction

The physics of transition metal oxides offers a wealth of interesting phenomena related to their strongly correlated nature. This is because the bandwidth is relatively small compared to the intraionic Coulomb repulsion between the $3d$ electrons. The understanding of many unique properties of oxides, such as high-T_c superconductivity and colossal magnetoresistivity is therefore based on the well-known Mott physics.[1]

Among the various families of transition metal oxides, attention has recently focused on layered cobaltates, in particular on the sodium cobaltate Na_xCoO_2. The interest was initiated by the large thermoelectric power observed in this compound,[2]–[4] i.e. the capability of an efficient conversion of heat energy to electricity. The research on these systems was further boosted by the unexpected discovery of superconductivity (SC) in water-intercalated Na_xCoO_2.[5] Soon after, many remarkable properties were found[6] such as spin-sensitive thermopower,[3] unusual charge and spin orderings,[7]–[11] very narrow quasiparticle bands[12]–[16] and especially a very unusual phase diagram.[7] While the strongly correlated nature of Na_xCoO_2 is no longer at doubt, the mechanisms by which the correlated electrons design such an exotic phase diagram are not fully understood even on a qualitative level.

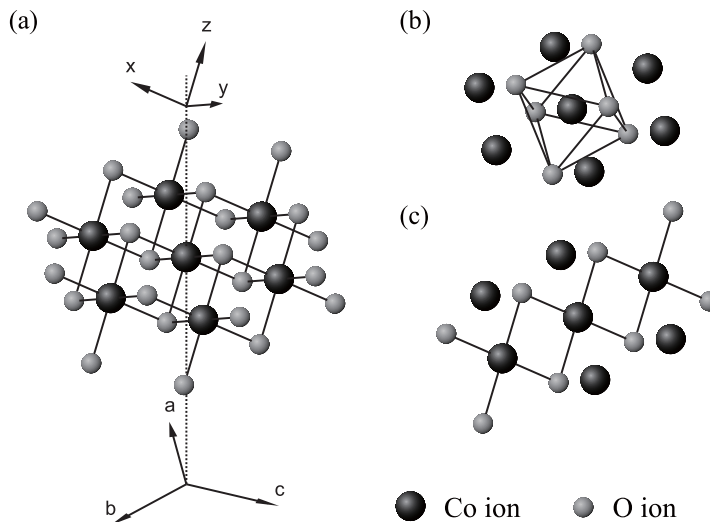Layered cobaltates consist of CoO_2 planes with a triangular lattice of Co ions

Fig. 1. (a) Structure of a hexagonal CoO_2 plane with $90°$ cobalt-oxygen bonds pointing along x, y and z directions. The directions in the hexagonal lattice of cobalt ions are denoted by a, b and c respectively. (b) Each cobalt ion is surrounded by six oxygen ions forming an octahedron, in the real structure this is slightly distorted. (c) Each cobalt ion is a member of three CoO_2 chains which determine planes perpendicular to the x, y and z axes respectively. In the figure, chain of b direction determining a plane perpendicular to the y axis is shown.

(see Fig. 1), separated either by Na layers as in $Na_x CoO_2$[7] or by BiO-BaO layers of rock-salt structure in so-called "misfit" cobaltates [see 16), 17) and references therein]. By suppressing electron motion along the c-axis these layers impose quasi-two-dimensionality upon the CoO_2 layers. In addition they provide the charge carriers to the CoO_2 planes in doped compounds. Depending on the composition, the valence state of Co ions may vary in a wide range from non-magnetic Co^{3+} t_{2g}^6 $S = 0$ state (as in $NaCoO_2$) towards the magnetic Co^{4+} t_{2g}^5 $S = 1/2$ configuration (in $Na_x CoO_2$ at small x).

The Co^{3+} systems where the cobalt ions have full t_{2g}^6 shell are naturally referred to as band insulators,[18], [19] whereas in Co^{4+} $S = 1/2$ rich systems strongly correlated Mott behavior is expected. Thus by reducing sodium content in $Na_x CoO_2$ one should be able to observe an evolution from the weakly correlated band-insulator regime to a doped Mott limit. However, the experiments show completely opposite trends. The Co^{4+} rich compounds are just moderately correlated metals[7], [20] while Co^{3+} rich compositions show signatures of strong correlations such as magnetic order,[7], [9] strong magnetic field effects,[3] etc. Pronounced incoherent structures in the angular-resolved photoemission (ARPES) spectra[16], [21] revealing the complex structure of holes doped into $NaCoO_2$ are also enhanced near the band-insulator limit.

Even more puzzling situation occurs with hydration of $Na_x CoO_2$. Depending on the amount of water intercalating the structure, $Na_x CoO_2$ forms a monolayer hydrate or (at a larger water content) a bilayer hydrate[22], [23] (see Fig. 2 for the details of the structure). As a big surprise, superconductivity was discovered in the bilayer hydrate of $Na_x CoO_2$ with $x \approx 0.35$.[5] The corresponding transition temperature is quite low
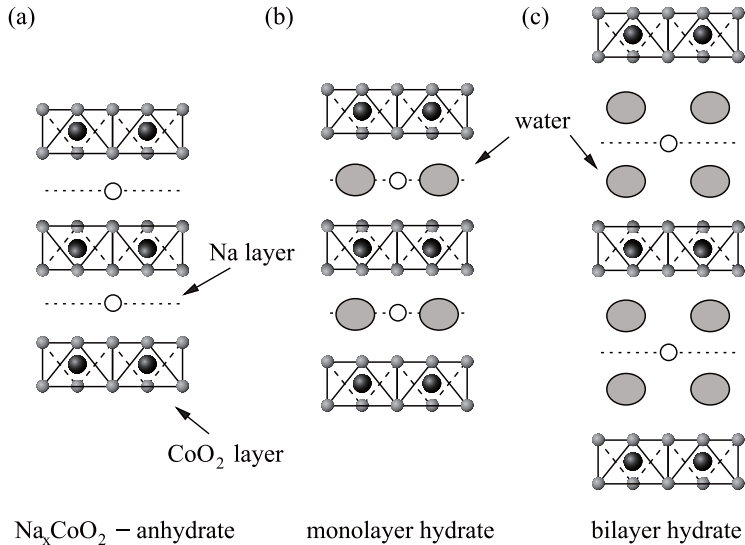
Fig. 2. Layered structure of (a) anhydrate Na_xCoO_2 and water-intercalated (b) monolayer hydrate, (c) bilayer hydrate. Water-intercalation leads to an expansion in the direction normal to CoO_2 planes and in the case (c) brings a large screening of sodium potential.

— $T_c \simeq 5K$ in the optimal case. However, the identification of the pairing mechanism is a problem of principal importance, because this may shed some light on the other mysteries of Na_xCoO_2 as well. Soon after the discovery, comparisons with the cuprate situation have been made.[5),24)] They emphasize the quasi-two-dimensional CoO_2 layers of $S = 1/2$ background (Co^{4+} ions) doped by $S = 0$ (Co^{3+} ions) charge carriers, thereby representing a t_{2g} analog of CuO_2 planes. The triangular lattice of Co ions might be convenient for a realization of resonating-valence-bond (RVB) state,[25)] which was originally proposed for a $S = 1/2$ Heisenberg antiferromagnet on a triangular lattice.[26)] Despite this, it was quickly realized, that the phase diagram of Na_xCoO_2[7)] is radically different from that of cuprates. As already mentioned, the enhanced strongly correlated nature is rather observed at high relative content of *nonmagnetic* Co^{3+} ions. Also the location of the superconducting dome initially expected at cobalt valency around 3.65 (as in $Na_{0.35}CoO_2$) was later found at actual valency ~ 3.4, closer to the Co^{3+} situation due to water-induced valency shift.[27)–29)]

Many-body effects observed near a band insulator regime of cobaltates are puzzling and indicate that electronic correlations originate from a specific mechanism different from that of the cuprates. We have recently proposed a model[30),31)] for strong correlations that operate over the entire phase diagram of Na_xCoO_2 including a weakly doped band insulator limit. In this paper, we discuss this model and its predictions in more detail, and further extend it to the case of multiorbital situation.

Considering the limit of diluted $S = 1/2$ Co^{4+} holes doped into non-magnetic band insulators $NaCoO_2$ and misfit cobaltates, the model predicts a polaronic behavior of the holes characterized by strongly reduced quasiparticle peaks and dispersive incoherent structures in their spectral functions. In the Fermi-liquid regime at large concentration of the doped holes, a specific pairing mechanism driven by correlated
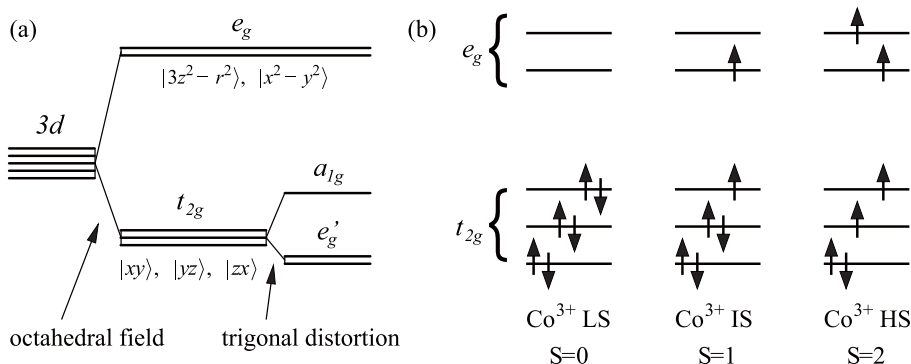
Fig. 3. (a) $3d$ levels of cobalt ions split into t_{2g} and e_g levels in the octahedral field of oxygen ions. Trigonal distortion leads to a further splitting among the t_{2g} orbitals. The order of the resulting a_{1g} and e'_g levels shown corresponds to that suggested by ARPES experiments in Na_xCoO_2. (b) Low-spin, intermediate-spin, and high-spin states of Co^{3+} ions. The competition between the t_{2g}-e_g crystal field splitting favoring t_{2g}^6 configuration and the Hund coupling favoring higher spin values makes them quasidegenerate.

hopping of doped holes emerges in the model. The resulting SC is optimized near the cobalt valency 3.4 in agreement with experimental observations. The model is based on a unique aspect of Co^{3+} ions, i.e., their spin-state quasidegeneracy, and on special lattice geometry of CoO_2 layers realized in the layered cobaltates.

Let us first consider the $3d$ electrons of cobalt ions from a single electron point of view as shown in Fig. 3(a). The individual cobalt ions are in octahedral crystal field [Fig. 1(b)] which leads to the usual t_{2g}-e_g splitting $10Dq$ like in a perovskite structure. Due to the layered structure of cobaltates, which imposes a quasi-two-dimensionality of the electronic states, the symmetry of the originally three-fold degenerate t_{2g} levels is thus lowered and they split into so-called a_{1g} and e'_g states. Crystal field prefers the t_{2g}^5 configuration on the Co^{4+} ions. The holes doped into $NaCoO_2$ or misfits are then expected to occupy the highest t_{2g} level. Initially, theoretical considerations have suggested that this level should be of e'_g symmetry (see Ref. 32) for details). However, experiments support an opposite scenario where the doped holes prefer to occupy the a_{1g} orbital states. Indeed, ARPES data shows a very simple Fermi surface derived from a single band of a_{1g} symmetry.[16), 21)]

In the case of Co^{3+}, the t_{2g}^6 $S = 0$ configuration would be selected by the cubic crystal-field splitting $10Dq$ alone. However, many-body effects represented by the Hund coupling favoring high-spin configurations compete with the crystal field splitting, making the $S = 0$, $S = 1$ and $S = 2$ states of Co^{3+} quasidegenerate [Fig. 3(b)]. Spin-state quasidegeneracy of cobalt ions is well known, $LaCoO_3$ being a textbook example.[33)] According to Ref. 34), magnetic states are in the range of $\sim 200 - 400\,\mathrm{meV}$ ($S = 1$) and $\gtrsim 50\,\mathrm{meV}$ ($S = 2$) above the t_{2g}^6 $S = 0$ ground state (without lattice relaxations). This leads to a distinct property of Co^{3+} rich oxides called "spin-state-transition" responsible for many anomalies such as spin-state changes in $LaCoO_3$,[34), 35)] and a spin-blockade effect in $HoBaCo_2O_{5.5}$,[36)] to mention a few manifestations of the Janus-like behavior of Co^{3+}.

In the groundstate the cobalt ions are supposed to be in $S = 1/2$ Co^{4+} or $S = 0$ Co^{3+} states. Thanks to the spin-state quasidegeneracy, a new, third degree of freedom — namely the low-lying $S = 1$ $t_{2g}^5 e_g^1$ state of Co^{3+} — could be in principle employed by intersite t_{2g}-e_g hopping which mixes the t_{2g}^6 and $t_{2g}^5 e_g^1$ configurations of neighboring ions.[*] Whether such a matrix element is finite or not depends on lattice geometry. With the $180°$ Co-O-Co bond geometry of perovskite cobaltates, the t_{2g} and e_g sectors are separated with respect to the nearest-neighbor hopping [see Fig. 4(a) for an explanation], which is therefore incapable to produce the $S = 1$ Co^{3+} states. A new situation encountered in layered cobaltates is that CoO_6 octahedra are edge-shared. In this geometry, the hopping occurs along the $90°$ Co-O-Co bonds, where the largest matrix element is that between the orbitals of t_{2g} and e_g symmetry as shown in Fig. 4(b). Doped holes can now easily generate $S = 1$ $t_{2g}^5 e_g^1$ states of Co^{3+} which become strongly coupled to the groundstate by virtue of intersite t_{2g}-e_g electron transfer. In other words, the magnetic configuration of Co^{3+} is activated once the mobile Co^{4+} holes are added in $Na_x CoO_2$. A dynamical generation of $t_{2g}^5 e_g^1$ $S = 1$ states by a hole motion converts it into a many-body correlated object — the spin-polaron. At larger density of Co^{4+} when spin-polarons overlap, the virtual $S = 1$ states act as mediators of an effective spin-sensitive interaction. We eliminate these
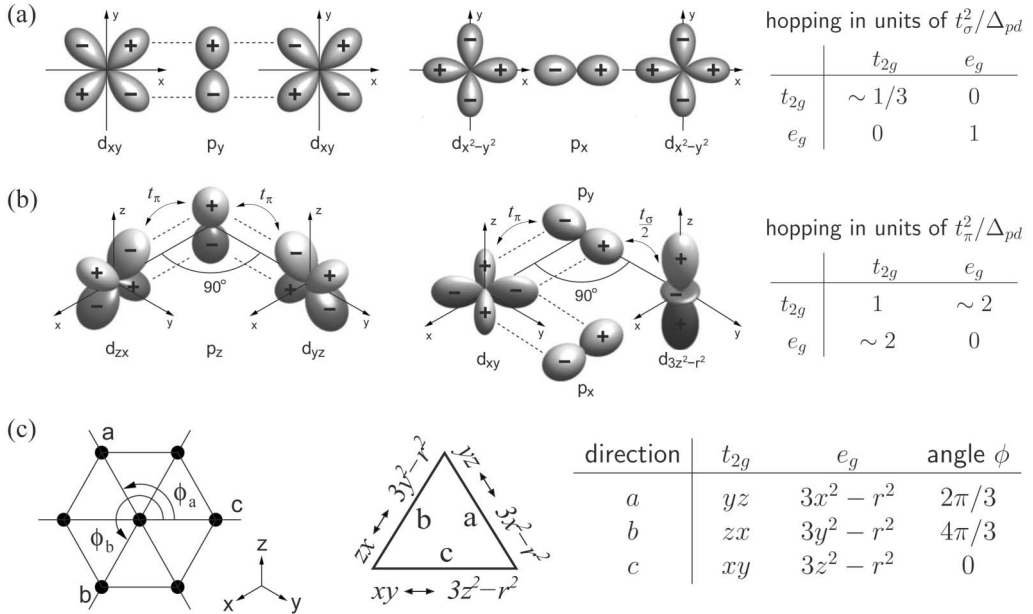

Fig. 4. (a) Hopping between d-orbitals of cobalt ions via oxygen ions in the case of $180°$ Co-O-Co bonds. The geometry allows for the nearest-neighbor t_{2g}-t_{2g} and e_g-e_g hopping. The t_{2g} and e_g sectors are independent. (b) The same for the $90°$ Co-O-Co bonds as in $Na_x CoO_2$. Nearest-neighbor t_{2g}-t_{2g} and t_{2g}-e_g hopping is possible, the latter one being approximately two times stronger. (c) a, b and c directions in the hexagonal lattice of cobalt ions and orbitals connected by the t_{2g}-e_g hopping along the three directions.

[*] The $S = 2$ Co^{3+} configuration with two e_g electrons is not accessible by the t_{2g}-e_g hopping.

virtual states perturbatively, and find an effective model in a form of spin-selective pair hopping of electrons. The correlated hopping energy is optimized when holes are paired and condense into a SC state.

A résumé is that low-lying magnetic states of Co^{3+}, accessible for electrons via the intersite hopping, provide an extra dimension in physics of $Na_x CoO_2$. In §2, we design a model incorporating this idea. Based on this model, we demonstrate in §3 that holes doped into the band insulator $NaCoO_2$ behave in fact as magnetic polarons dressed by the spin-state fluctuations of Co^{3+} ions that are excited by the hole motion. Section 4 derives the effective interaction between holes, mediated by virtual spin-state excitations of Co^{3+} ions, in a Fermi-liquid regime at larger hole densities. In §5, we discuss the relevance of these interactions to the spin ordering, and, by exploring their effect on the spin susceptibility, we find signatures of $2k_F$-instabilities. Finally, we focus in §§6 and 7 on the superconductivity within our model. First, in §6 we discuss symmetry and doping dependencies of pairing instabilities in the model based on the a_{1g} band only. To address a possible role of e'_g pockets in the superconductivity, in §7 we extend the model by employing the full orbital structure of the relevant states. Section 8 concludes the paper.

§2. Model Hamiltonian

The t_{2g} orbitals in $Na_x CoO_2$ split into single $a_{1g} = (d_{xy} + d_{yz} + d_{zx})/\sqrt{3}$ state and two e'_g states: $e'_{g1} = (d_{yz} - d_{zx})/\sqrt{2}$ and $e'_{g2} = (2d_{xy} - d_{yz} - d_{zx})/\sqrt{6}$. The photoemission experiments[12)–14), 16)] show that a single band, derived mostly from the a_{1g} orbitals, is active near the Fermi level [see Ref. 37) for possible orbital-selection mechanism]. Therefore, we consider first a model based on the $a_{1g} \equiv f$ hole states (the version containing also e'_g orbitals will be introduced in §7). Valence fluctuations $d_j^6 d_i^5 \to d_j^5 d_i^6$ (see the left part of Fig. 5) within the low-spin t_{2g} manifold are described by the tight-binding Hamiltonian

$$H_t = -t \sum_{ij\sigma} f^{\dagger}_{j\sigma} f_{i\sigma} \, , \tag{2.1}$$

where $t = 2t_0/3$ and $t_0 = t_\pi t_\pi /\Delta_{pd}$ is the overlap between t_{2g} orbitals[38)] (hereafter, a hole representation is used). The fermionic operators f are subject to a conventional Gutzwiller constraint (at most one hole at a given site). As a result the bandwidth following from (2.1) is reduced by the Gutzwiller factor $g_t = 2n_d/(1 + n_d)$ ($\approx n_d$ at the relevant dopings). Here n_d is the relative fraction of Co^{3+} ions.

Our crucial observation following from Fig. 4(b) is that the t_{2g}-e_g hopping $\tilde{t} = t_\sigma t_\pi /\Delta_{pd}$, which uses a stronger σ-bonding path with $t_\sigma /t_\pi \sim 2$, leads to more effective valence fluctuations. These will constitute the second part, $H_{\tilde{t}}$, of our model Hamiltonian: $H_{t-\tilde{t}} = H_t + H_{\tilde{t}}$. The $\tilde{t}$ process (Fig. 5) generates $S = 1$ state of Co^{3+} composed of a t_{2g} hole and an e_g electron. Low-spin $S = 0$ $t_{2g}^5 e_g^1$ state is much higher in energy and can be ignored (see §7 for details on the $t_{2g}^5 e_g^1$ multiplet structure of Co ions). We represent the resulting state by the operator $\mathcal{T}$ specified by the spin projection of the $S = 1$ state and the e_g orbital γ created by $\tilde{t}$ hopping,
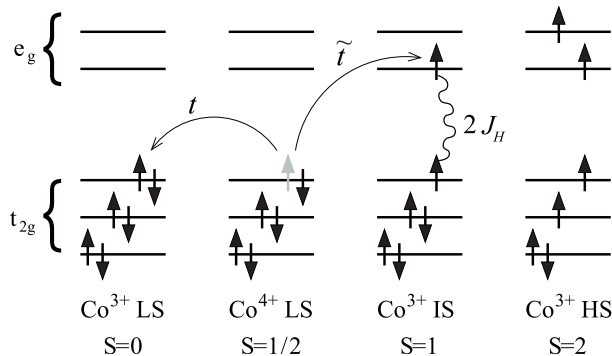
Fig. 5. Processes contained in the t-$\tilde{t}$ model. Usual t-hopping gives rise to the band structure. $\tilde{t}$-hopping allows to employ the low-lying triplet state of Co^{3+}. High-spin ($S = 2$) state is not accessible by hopping.

i.e., $\mathcal{T}_{+1,\gamma}^{\dagger} = \overline{e_{\gamma\uparrow}^{\dagger} f_{\uparrow}^{\dagger}}$, $\mathcal{T}_{-1,\gamma}^{\dagger} = \overline{e_{\gamma\downarrow}^{\dagger} f_{\downarrow}^{\dagger}}$ and $\mathcal{T}_{0,\gamma}^{\dagger} = \overline{(e_{\gamma\uparrow}^{\dagger} f_{\downarrow}^{\dagger} + e_{\gamma\downarrow}^{\dagger} f_{\uparrow}^{\dagger})}/\sqrt{2}$. The e_g orbital is selected by the hopping geometry depicted in Fig. 4(b). The nearest-neighbor Co ions and two O ions binding them determine a plane [see Fig. 1(c)] which is labeled as a, b or c according to the Co-Co bond direction. With respect to this plane, the $\tilde{t}$-hopping couples the in-plane t_{2g} orbital to the out-of-plane e_g orbital. This rule is shown in Fig. 4(c). For the $\tilde{t}$ hopping along a, b, or c bond, $\gamma = 3x^2 - r^2$, $3y^2 - r^2$ or $3z^2 - r^2$ respectively. The $H_{\tilde{t}}$ part of our minimal model Hamiltonian for Na_xCoO_2 reads then as[30]

$$H_{\tilde{t}} = -\frac{\tilde{t}}{\sqrt{3}} \sum_{ij} \left[\mathcal{T}_{+1,\gamma}^{\dagger}(i) f_{j\downarrow}^{\dagger} f_{i\uparrow} - \mathcal{T}_{-1,\gamma}^{\dagger}(i) f_{j\uparrow}^{\dagger} f_{i\downarrow} - \mathcal{T}_{0,\gamma}^{\dagger}(i) \frac{1}{\sqrt{2}} \left(f_{j\uparrow}^{\dagger} f_{i\uparrow} - f_{j\downarrow}^{\dagger} f_{i\downarrow} \right) + \text{h.c.} \right].$$

$$(2\cdot2)$$

The factor of $1/\sqrt{3}$ comes from the projection onto the a_{1g} band within t_{2g} sector. $H_{\tilde{t}}$ moves an electron from Co_j^{3+} to Co_i^{4+} — producing a t_{2g} hole on site j — and replaces the t_{2g} hole on site i by a complex excitation $\mathcal{T}$. Making use of the t_{2g}-e_g hopping (the *largest* one for 90° Co-O-Co bonds), an electron "picks-up" the spin correlations present in virtual $S = 1$ states.

The index γ of the $\mathcal{T}$ excitation is determined by the orientation of the $\langle ij \rangle$ bond according to the rules in Fig. 4(c). The overlap between e_g orbitals specified by γ and γ' is $\langle \gamma | \gamma' \rangle = \cos(\phi_\gamma - \phi_{\gamma'})$. Consequently, the excitations $\mathcal{T}_\gamma$ inherit the same overlap: $\langle \mathcal{T}_\gamma \mathcal{T}_{\gamma'}^{\dagger} \rangle \propto \langle \gamma | \gamma' \rangle$. This brings peculiar geometrical factors into the theory, as will be observed in the following sections.

The $\mathcal{T}$-excitation energy E_T is determined by all the many-body interactions within the CoO_6 complex (Hund's coupling, $p - d$ covalency, crystal field, ...).[34] This is a free parameter of the model. Experimentally, $S = 1$ states of CoO_6 complex in perovskite compound $LaCoO_3$ are found at energies $E_T \sim 0.2 - 0.4$ eV[34] as already mentioned in the Introduction. Based on this observation, we will use in this paper the representative value $E_T \simeq 0.2 - 0.3$ eV for layered cobaltates. In units of the a_{1g} hopping integral $t \simeq 0.1$ eV (which follows from the band structure fit $t_0 \simeq 0.15$ eV[37]), this translates into $E_T/t = 2 - 3$ adopted below in our numerical

data. In principle, we expect some material dependence of E_T as it is decided by the balance of several competing interactions. It is therefore highly desirable to quantify a multiplet structure of the CoO$_6$-complex in Na$_x$CoO$_2$ as done in LaCoO$_3$.[34)] For the ratio of the hopping amplitudes $\tilde{t}$ and t_0, we set $\tilde{t}/t_0 = 2$ as $t_\sigma/t_\pi \sim 2$.

§3. Spin-state polaron behavior of quasiparticles

Based on the model introduced in the previous section, we develop now a theory for the photoemission spectra in cobaltates at large sodium content. The concentration of the Co^{4+} holes doped into originally non-magnetic band insulator NaCoO$_2$ is small, so that we consider here the individual motion of the holes only. It is evident from the Hamiltonian (2·2), that by creating and destroying $\mathcal{T}$ excitations as they propagate, the holes are strongly renormalized and we deal with a spin-polaron problem. This resembles the problem of doped Mott insulators like cuprates, however, the nature of spin excitations is different here because of the nonmagnetic ground state. Instead of magnon-like propagating modes as in cuprates, fluctuations of the very spin value of Co^{3+} ions are the cause of the spin-polaron physics in cobaltates. In contrast to Refs. 39) and 40), where a *static* hole surrounded by $S = 1$ Co^{3+} ions was studied, in the present model the triplet $S = 1$ excitations are *virtual* and generated dynamically by the *very motion* of the hole via the $\tilde{t}$ process. These two pictures can merge if a hole is strongly trapped (e.g., by Na-potential[41)]).

For the calculation of the fermionic selfenergies, we employ the self-consistent Born approximation, which has extensively been used in the context of spin-polarons in cuprates.[42)] First, we focus on spin excitation spectrum. Since a direct e_g-e_g hopping in case of 90°-bonds is not allowed by symmetry, the bare $\mathcal{T}$ spin excitation is a purely local mode, at the energy E_T. The coupling to the holes in (2·2) shifts and broadens this level. Accounting for this effect perturbatively [see Fig. 6(a) for a diagrammatic representation], we obtain the $\mathcal{T}$ Green's function $\mathcal{D}^{-1}(i\omega) = i\omega - E_T - \Sigma_T(i\omega)$ with

$$\Sigma_T(i\omega) = \frac{2\tilde{t}^2}{3\beta} \sum_{\boldsymbol{k}\boldsymbol{k}',i\epsilon} \Gamma_{\boldsymbol{k}}\, \mathcal{G}_0(\boldsymbol{k}, i\epsilon)\mathcal{G}_0(\boldsymbol{k}', i\epsilon + i\omega) \ . \tag{3·1}$$

Here, $\mathcal{G}_0$ is the bare electron propagator $\mathcal{G}_0(\boldsymbol{k}, i\epsilon) = (i\epsilon - \xi_{\boldsymbol{k}})^{-1}$ with the a_{1g} dispersion on a triangular lattice $\xi_{\boldsymbol{k}} = -2t(c_a + c_b + c_c) + \mu$, where $c_\gamma = \cos k_\gamma$ and k_γ are the projections of $\boldsymbol{k}$ on the directions a, b, c. The underlying E_g symmetry of $\mathcal{T}$ operators involved in $\tilde{t}$ hopping results in the factor $\Gamma_{\boldsymbol{k}} = c_a^2 + c_b^2 + c_c^2 - c_a c_b - c_b c_c - c_c c_a$. We neglected a weak momentum dependence of Σ_T for the sake of simplicity. This is justified as long as Σ_T is small compared to the spin gap E_T.

Further, we approximate $\Gamma_{\boldsymbol{k}}$ by its Brillouin-zone average $3/2$, obtaining the simple expressions for Σ_T in terms of bare fermionic density of states $N_0(x) = \sum_{\boldsymbol{k}} \delta(x - \xi_{\boldsymbol{k}})$:

$$\mathrm{Im}\Sigma_T(E) = -\pi\tilde{t}^2 \int_{-E}^{0} \mathrm{d}x\, N_0(x)N_0(x + E) \ , \tag{3·2}$$
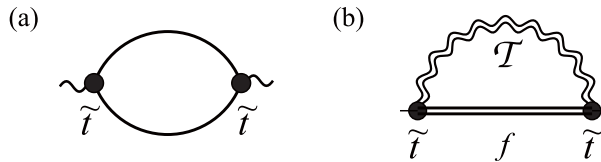
Fig. 6. (a) Selfenergy of the $\mathcal{T}$ excitation in the lowest order approximation. Solid lines represent bare hole propagator. (b) Selfenergy of the holes in a self-consistent Born approximation. The double straight line is the full hole propagator. The double wiggly line represents the propagator of the $\mathcal{T}$ excitation renormalized by the selfenergy in (a). (After Ref. 31).)

$$\mathrm{Re}\Sigma_T(E) = -\tilde{t}^2 \int_{-\infty}^0 dx \int_{x^2}^{\infty} dy^2 \, \frac{N_0(x)N_0(x+y)}{y^2 - E^2} \,. \tag{3.3}$$

These equations determine the renormalized spectral function of the spin-triplet excitation: $\rho_T(E) = -\pi^{-1}\mathrm{Im}\mathcal{D}(i\omega \to E + i\delta)$. Next, we use $\rho_T(E)$ below for calculation of the fermionic selfenergy.

Holes are renormalized by creating and destroying $S = 1$ Co^{3+} excitations while moving in the predominantly Co^{3+} background. The selfenergy diagram in a self-consistent Born approximation accounting for this effect [Fig. 6(b)] reads as:

$$\Sigma_{\boldsymbol{k}}(i\epsilon) = -\frac{2\tilde{t}^2}{\beta} \sum_{\boldsymbol{k}', i\omega} \left[\Gamma_{\boldsymbol{k}'}\mathcal{D}(-i\omega) + \Gamma_{\boldsymbol{k}}\mathcal{D}(i\omega) \right] \mathcal{G}(\boldsymbol{k}', i\epsilon + i\omega) \,, \tag{3.4}$$

where $\mathcal{G}^{-1}(\boldsymbol{k}, i\epsilon) = i\epsilon - \xi_{\boldsymbol{k}} - \Sigma_{\boldsymbol{k}}(i\epsilon)$. We can decompose the $\boldsymbol{k}$-dependence of the selfenergy into two simple terms and write $\Sigma_{\boldsymbol{k}}(\omega) = 2\tilde{t}^2[\Phi(\omega) + \Gamma_{\boldsymbol{k}}\Xi(\omega)]$, where

$$\Phi(\omega) = \int_0^{\infty} dE \, \rho_T(E) \int_0^{\infty} dx \, \frac{\tilde{N}(x)}{\omega - E - x + i\delta} \,, \tag{3.5}$$

$$\Xi(\omega) = \int_0^{\infty} dE \, \rho_T(E) \int_{-\infty}^0 dx \, \frac{N(x)}{\omega + E - x + i\delta} \,. \tag{3.6}$$

The full local density of states $N(E) = \sum_{\boldsymbol{k}} A(\boldsymbol{k}, E)$ and its E_g symmetry part $\tilde{N}(E) = \sum_{\boldsymbol{k}} \Gamma_{\boldsymbol{k}} A(\boldsymbol{k}, E)$ are functions of the selfenergy itself, via the spectral functions $A(\boldsymbol{k}, E) = -\pi^{-1}\mathrm{Im}\mathcal{G}(i\epsilon \to E + i\delta)$. The above equations are thus to be solved self-consistently.

The reliability of the approximations made was tested by the comparison with an exact diagonalization of $H_{t-\tilde{t}}$. Considering a single hole injected on a 7-site hexagonal cluster, it was shown in Ref. 31), that the above equations give results consistent with the exact diagonalization, even at rather small spin gap values $E_T \sim t$.

To illustrate the gross features of the hole renormalization, in Fig. 7 we show a complete map of the spectral function along M-Γ-K path in the Brillouin zone and spectral profiles at selected points. We have used a representative value $E_T = 2t$ which is renormalized by holes to $\tilde{E}_T \approx 1.4t$. Renormalization of the holes leads to spectral functions with a reduced quasiparticle (qp-) peak whose spectral weight is transferred to a pronounced hump structure. [A peculiar momentum dependence of the matrix elements $\Gamma_{\boldsymbol{k}}$ (note that $\Gamma_{\boldsymbol{k}=0} = 0$) reduces the effect at $\boldsymbol{k} = \Gamma$ point].
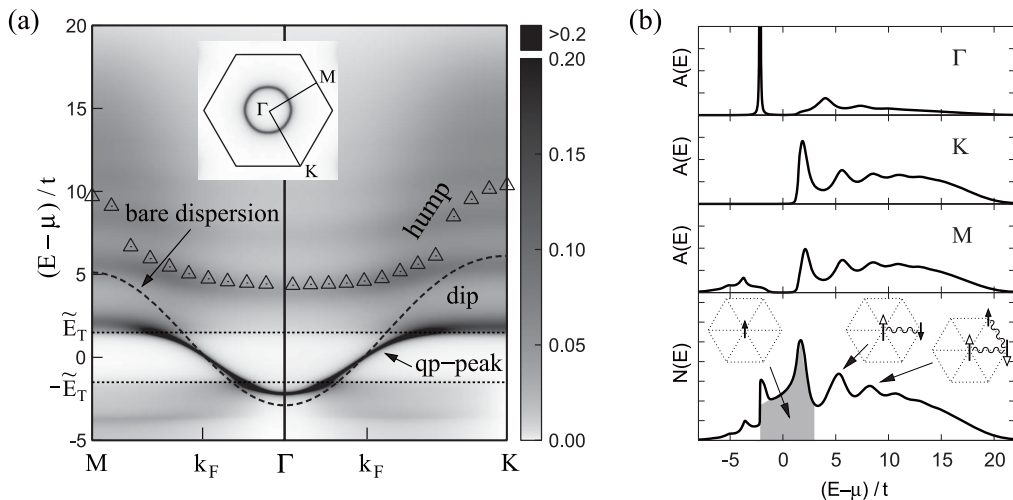
Fig. 7.   (a) Intensity map of the spectral function $A(\boldsymbol{k}, E)$ of the Co^{4+} holes along the M-Γ-K path in the hexagonal Brillouin zone (inset) calculated at 30% doping and $E_T = 2t$. Near the Fermi level, the quasiparticle (qp-) peak is well developed. As the hole energy reaches the renormalized $\mathcal{T}$ excitation energy $\tilde{E}_T$, the quasiparticle peak broadens and its weight is transferred to a broad, incoherent background. This results in a "peak-dip-hump" profile of the spectral function as seen in the right panel. The top of the smoothed hump structure is indicated by triangles. The dashed line shows the bare dispersion. (b) Spectral function profiles at the Γ, K and M points and the total density of states $N(E)$. The incoherent structure dominates $N(E)$, a small coherent part resembling the density of states of the bare band (with a reduced bandwidth) is indicated by the gray area. Several maxima on the hump structure reflect the presence of multiple $\mathcal{T}$ excitations as sketched in the cartoon figures. (After Ref. 31).)

Compared to the bare dispersion, the bandwidth of the renormalized holes is reduced by a factor ~ 2. The main observation here is that as the hole energy reaches $\tilde{E}_T$, the dynamical generation of $S = 1$ excitations becomes very intense and a broad incoherent response develops, leading to the pronounced "peak-dip-hump" structure of $A(\boldsymbol{k}, E)$. Several maxima on the hump reflect the presence of multiple triplet excitations created by the hole propagation. All these are the typical signatures of polaron physics. Multiplet structure of the hump will in reality be smeared by phonons which are naturally coupled to the $\tilde{t}$ transition involving also the orbital sector. Although experiments[43] indicate that electron-phonon coupling is moderate in cobaltates, it may enhance the spin-polaron effects as in cuprates.[44] Following the maximum of the smoothed hump structure, we observe its strong dispersion (stemming also from incoherent $\tilde{t}$ hopping).

Figure 7 suggests a possible determination of $\tilde{E}_T$ from the quasiparticle damping. To address this problem, in Fig. 8 we show the energy width of the qp-peak following its dispersion curve. The sharp onset of the damping at the binding energy $\approx -1.4t$ is clearly related to the maximum of the spin-excitation spectral function $\rho_T(E)$. In addition, Fig. 8 shows the weight of the qp-peak which is $\boldsymbol{k}$-dependent (mainly due to the matrix element $\Gamma_{\boldsymbol{k}}$).

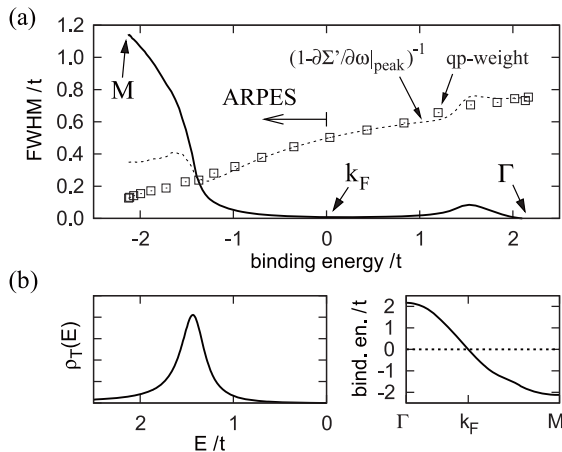Comparison of Figs. 7 and 8 with the data of Refs. 16) and 21) reveals a re-

(a)

(b)

Fig. 8. Top panel: Full energy width at half maximum of the quasiparticle peak along the M-Γ dispersion curve (see bottom-right panel) plotted as a function of the binding energy. The part from k_F to M is accessible by ARPES experiments. Strong quasiparticle damping below $\sim -1.4t$ is due to a scattering on $S = 1$ excitations. The spectral weight of the quasiparticle peak obtained by a direct integration is indicated by squares. When damping is small, it coincides with a conventional quasiparticle residue $(1 - \partial \Sigma' / \partial \omega)^{-1}$. Lower panel: The $\mathcal{T}$-exciton spectral function (left), and renormalized hole dispersion (right). (After Ref. 31).)

markable correspondence between theory and experiment. In particular, both the qp-peak and the hump dispersions (see Figs. 2 and 3 of Ref. 16)) are well reproduced by theory, considering $t \approx 0.1$ eV suggested by the band structure fit.[37] The onset energy $\tilde{E}_T \sim 1.4t$ for the qp-damping (Fig. 8) is then ≈ 0.14 eV, in agreement with experiment (see Fig. 2(c) of Ref. 16)).

Physically, at large $x \sim 1$ limit, dilute polarons are readily trapped by a random potential of Na-vacancies,[41),45)] thus qp-peaks should be suppressed at low hole doping. When the binding is strong, physics is local and a polaron takes a form of hexagon-shaped $S = 1/2$ object where a hole is oscillating to optimize both t and $\tilde{t}$ channels.[39] Our model provides a microscopic basis for spin-polarons introduced on experimental grounds[8),11)] and discussed in detail in Refs. 39) and 40). When the density of polarons is increased (as x decreases), they start to overlap forming narrow bands. Eventually, the polaron picture breaks down and a correlated Fermi-liquid emerges when x is further reduced. This is the subject of the following section, where we develop a perturbative theory accounting for the interactions between the holes.

§4. Effective interaction between t_{2g} holes: single a_{1g} band case

In the Fermi liquid regime, the Eliashberg-formalism, where the phonon shake-up processes (triggered by $\mathcal{T}$-exciton) can also be incorporated, would be the best strategy. However, there are delicate constraints to handle: a lattice site cannot be occupied by two holes or by a hole and $\mathcal{T}$-excitation simultaneously. For the sake of simplicity, we derive an effective fermionic interaction in a second order
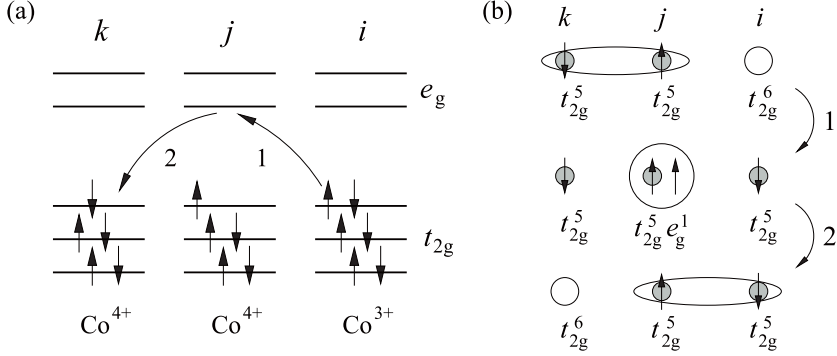
Fig. 9. (a) Virtual process leading to the H_P Hamiltonian in Eq. (4·1). t_{2g} electron of a Co_i^{3+} ion moves to e_g level of the nearest-neighbor Co_j^{4+} ion (process 1) and then to the t_{2g} level of the next Co_k^{4+} neighbor (process 2). This is depicted in (b) as a motion of the hole-pair. The intermediate state contains the low-lying $S = 1$ state of Co^{3+} ion. (After Ref. 30).)

perturbation theory in $\tilde{t}$ by considering the local virtual process depicted in Fig. 9. This way, all the constraints in the intermediate states are treated explicitly. Such a perturbative treatment is valid as long as a polaron binding energy E_b (an energy gain due to the $\tilde{t}$ process) is small compared to a bare bandwidth W ($\simeq 9t$ in a triangular lattice). From a self-consistent Born approximation discussed above, we obtained single polaron binding energy $E_b \simeq 2.6t$ ($2.9t$) for E_T set to the value $3t$ ($2t$) used in this paper. Hence, $E_b \sim 0.3W$ and we can integrate out virtual spin states perturbatively.

In the virtual process of Fig. 9 we consider an initial configuration with a pair of Co^{4+} holes and a $S = 0$ Co^{3+} state at the neighboring site. First $\tilde{t}$-hopping (i.e. the action of $H_{\tilde{t}}$) generates an excited $S = 1$ state surrounded by two Co^{4+} holes. The energy of this virtual state with respect to the initial state equals E_T. The virtual state gets deexcited by second $\tilde{t}$-hopping leaving the system again with a pair of holes and a neighboring Co^{3+} state. Since the pair now has a changed position, the virtual process effectively corresponds to the motion of the hole pair. The kinetic energy gain associated with this pair motion may lead to the pairing instability as shown in §6. Summing up the contributions of all possible virtual states, we arrive at the following effective Hamiltonian:

$$H_P = \sum_{\langle ijk \rangle} \left[P_{ijk}^S \hat{S}_{ij}^\dagger \hat{S}_{kj} + P_{ijk}^T \hat{\boldsymbol{T}}_{ij}^\dagger \hat{\boldsymbol{T}}_{kj} \right] . \tag{4·1}$$

The Hamiltonian in Eq. (4·1) describes the motion of the spin-singlet $\hat{S}_{ij} = (f_{i\uparrow}f_{j\downarrow} - f_{i\downarrow}f_{j\uparrow})/\sqrt{2}$ and spin-triplet $\hat{\boldsymbol{T}}_{ij} = \{f_{i\uparrow}f_{j\uparrow}, (f_{i\uparrow}f_{j\downarrow} + f_{i\downarrow}f_{j\uparrow})/\sqrt{2}, f_{i\downarrow}f_{j\downarrow}\}$ Co^{4+}-Co^{4+} pairs in a background of $S = 0$ Co^{3+} ions. Sites $i \neq k$ are the nearest neighbors of site j. No-double-occupancy constraint on f is implied when using this effective Hamiltonian. The pair-hopping amplitudes read as

$$P_{ijk}^S = \frac{1}{2}V \cos(\phi_{ij} - \phi_{kj}) , \quad P_{ijk}^T = \frac{1}{3}P_{ijk}^S . \tag{4·2}$$

We introduced here a parameter $V = \tilde{t}^2/E_T$ characterizing the interaction strength. The angles $\phi \in (2\pi/3, 4\pi/3, 0)$ are selected by the orientation of the bonds $\langle ij \rangle$ and $\langle jk \rangle$ as already explained in §2.

Two important remarks should be made on the pair-hopping amplitudes P_{ijk}. First, they contain a geometrical factor $\cos(\phi_{ij} - \phi_{jk})$ which equals $+1$ for straight pair hopping and $-1/2$ if the hopping process changes the direction of the pair. This factor is explained in Fig. 10. It originates from the fact, that different e_g orbitals participate in the $\tilde{t}$-hopping process on bonds of different directions. Second, the pair hopping amplitude of singlet pairs is three times as big as that of the triplet pairs. This nontrivial result originates from a quantum interference between different realizations of the virtual process as indicated in Fig. 11. The $S = 1$ intermediate state is fully transparent for singlets which equally use all three $S_z = \pm 1, 0$ states. However, these states contribute with different signs in case of triplets, resulting in a "spin blockade" for their motion.

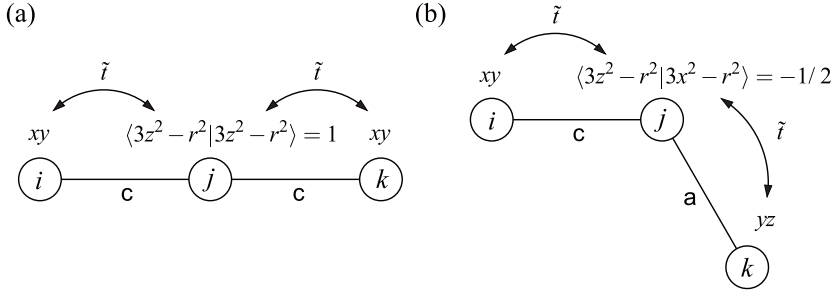Finally, the processes contained in the reduced model Hamiltonian $H_{t-P} =$

Fig. 10. The origin of the geometrical factor $\cos(\phi_{ij} - \phi_{jk})$ in Eq. (4·1) due to the overlap of the e_g orbitals in the intermediate state. (a) Along the c-bond, the xy and $3z^2 - r^2$ orbitals are coupled via $\tilde{t}$-hopping. If the virtual process of Fig. 9 proceeds along the c-bond exclusively, we get the geometrical factor $\cos(0) = 1$. (b) The bond-directions for the two $\tilde{t}$-hoppings differ. In the case of a-bond, the yz and $3x^2 - r^2$ orbitals are coupled via $\tilde{t}$-hopping. By taking the overlap of the e_g orbitals active on the two bonds, we get the geometrical factor $\cos(2\pi/3) = -1/2$.
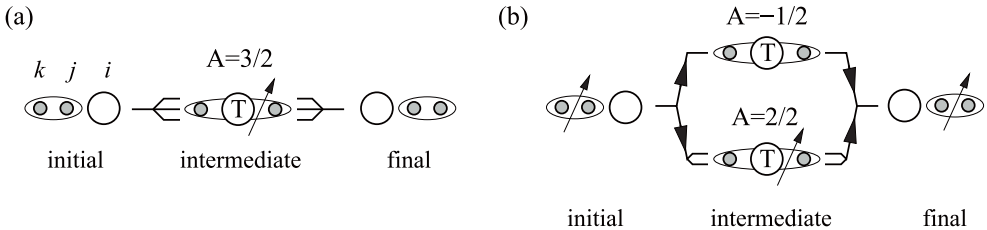

Fig. 11. (a) Singlet-pair motion via an intermediate state composed of $S = 1$ Co_j^{3+} ion ($\mathcal{T}$ exciton) and triplet state of the two holes at sites i and k. The process equally uses all three $S_z = \pm 1, 0$ states of Co^{3+}. The relative amplitude resulting from spin algebra equals 3/2. (b) The same for triplet-pair motion. Here the amplitude is distributed into two channels — with the two holes in the intermediate state being in singlet (one S_z state of Co^{3+} employed) or triplet state (two S_z states of Co^{3+} employed). Destructive interference of the two channels makes triplet-pair hopping amplitude 3 times as small as that of the singlet-pair.
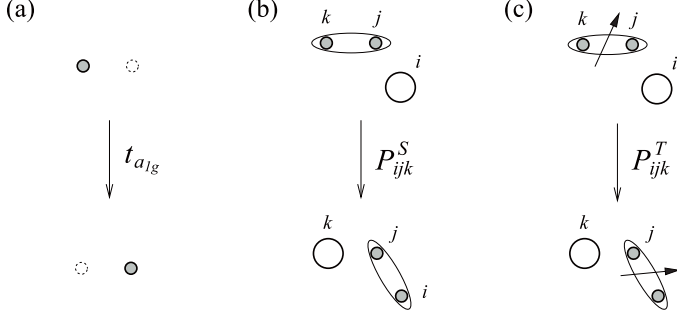
Fig. 12. Cartoon representation of the processes contained in the t-P Hamiltonian (2·1)+(4·1): (a) t-hopping of a_{1g} holes, (b) pair-hopping of a singlet pair of holes, and (c) pair-hopping of a triplet pair of holes.

$H_t + H_P$, Eqs. (2·1) and (4·1), are summarized in a concise way in Fig. 12. In the following sections we will use this model containing: 1. the usual t-hopping of holes [Fig. 12(a)] and 2. pair-hopping of hole pairs [Figs. 12(b) and (c)] as the lowest-order effect of $\tilde{t}$-hopping.

§5. Spin susceptibility

The pair-hopping interaction in Eq. (4·1) may be alternatively represented in a form of density-density and spin-spin couplings, emphasizing its relevance also to the charge and spin orderings:

$$H_P = V \sum_{\langle ijk \rangle} \cos(\phi_{ij} - \phi_{jk}) \left[n_j n_{ik} - \tfrac{1}{3} \boldsymbol{s}_j \boldsymbol{s}_{ik} \right] . \tag{5·1}$$

Here $n_j = \frac{1}{2} \sum_\sigma f_{j\sigma}^\dagger f_{j\sigma}$ and $\boldsymbol{s}_j^z = \frac{1}{2} \sum_\sigma \sigma f_{j\sigma}^\dagger f_{j\sigma}$ are the usual on-site charge and spin-density operators, but n_{ik} and $\boldsymbol{s}_{ik}$ with $i \neq k$ are the charge and spin densities residing on bonds, i.e., $n_{ik} = \frac{1}{2} \sum_\sigma f_{i\sigma}^\dagger f_{k\sigma}$, $\boldsymbol{s}_{ik}^z = \frac{1}{2} \sum_\sigma \sigma f_{i\sigma}^\dagger f_{k\sigma}$. Thus, the interaction acts between the local (*on-site*) and non-local (*bond*) operators which is a consequence of its three-site nature.

In momentum space, Eq. (5·1) can be written as

$$H_P = 2V \sum_{\boldsymbol{q}} \left[n_{-\boldsymbol{q}} \tilde{n}_{\boldsymbol{q}} - \tfrac{1}{3} \boldsymbol{s}_{-\boldsymbol{q}} \tilde{\boldsymbol{s}}_{\boldsymbol{q}} \right] , \tag{5·2}$$

with the usual operators $n_{\boldsymbol{q}} = \frac{1}{2} \sum_{\boldsymbol{k},\sigma} f_{\boldsymbol{k}+\boldsymbol{q},\sigma}^\dagger f_{\boldsymbol{k},\sigma}$, $s_{\boldsymbol{q}}^z = \frac{1}{2} \sum_{\boldsymbol{k},\sigma} \sigma f_{\boldsymbol{k}+\boldsymbol{q},\sigma}^\dagger f_{\boldsymbol{k},\sigma}$, and the momentum counterparts of the non-local operators $\tilde{n}_{\boldsymbol{q}} = \frac{1}{2} \sum_{\boldsymbol{k},\sigma} F_{\boldsymbol{k}+\boldsymbol{q},\boldsymbol{k}} f_{\boldsymbol{k}+\boldsymbol{q},\sigma}^\dagger f_{\boldsymbol{k},\sigma}$, $\tilde{s}_{\boldsymbol{q}}^z = \frac{1}{2} \sum_{\boldsymbol{k},\sigma} \sigma F_{\boldsymbol{k}+\boldsymbol{q},\boldsymbol{k}} f_{\boldsymbol{k}+\boldsymbol{q},\sigma}^\dagger f_{\boldsymbol{k},\sigma}$. The formfactor $F_{\boldsymbol{k}',\boldsymbol{k}} = \cos(k_a + k_a') + \cos(k_b + k_b') + \cos(k_c + k_c') - c_a c_b' - c_b c_a' - c_b c_c' - c_c c_b' - c_c c_a' - c_a c_c'$, where $c_\alpha' = \cos k_\alpha'$, originates from a peculiar bond-dependence of interactions in Eq. (5·1). It manifests again that the $\tilde{n}_q$ and $\tilde{\boldsymbol{s}}_q$ operators correspond to the particle-hole excitations that modulate the charge and spin bonds, respectively.
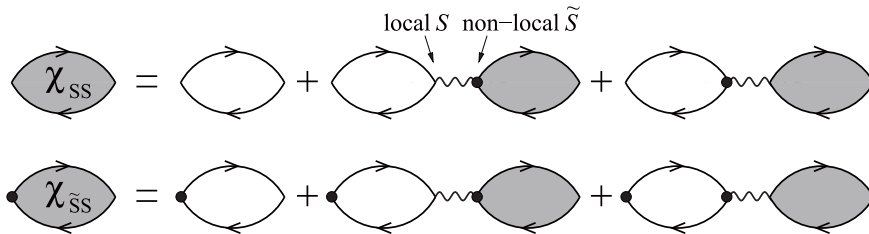
Fig. 13. Diagrammatic representation of RPA equations (5·4) for the spin susceptibilities involving the interaction (5·2) between local (s_q) and non-local ($\tilde{s}_q$) spin densities that reside on sites and bonds respectively. Bare and RPA enhanced susceptibilities are represented by empty and shaded bubbles, respectively.

To illustrate this unusual, nonlocal nature of correlations we investigate the effect of the interaction on the spin susceptibility within the RPA approximation. The bare spin susceptibility χ_{ss} is given by the formula

$$\chi_{ss}^{(0)}(\boldsymbol{q},\omega) = \frac{1}{4}\sum_{\boldsymbol{k}} \frac{\tanh(\xi_{\boldsymbol{k}}/2T) - \tanh(\xi_{\boldsymbol{k}+\boldsymbol{q}}/2T)}{\omega + \xi_{\boldsymbol{k}} - \xi_{\boldsymbol{k}+\boldsymbol{q}} + i\delta} \ . \tag{5·3}$$

A diagrammatic representation of the RPA approximation in our case of local-nonlocal spin interaction is shown in Fig. 13. RPA enhanced susceptibility follows from the equations

$$\chi_{ss} = \chi_{ss}^{(0)} + \Lambda\chi_{ss}^{(0)}\chi_{\tilde{s}s} + \Lambda\chi_{s\tilde{s}}^{(0)}\chi_{ss} \ ,$$
$$\chi_{\tilde{s}s} = \chi_{\tilde{s}s}^{(0)} + \Lambda\chi_{\tilde{s}s}^{(0)}\chi_{\tilde{s}s} + \Lambda\chi_{\tilde{s}\tilde{s}}^{(0)}\chi_{ss} \ , \tag{5·4}$$

where we defined a coupling constant $\Lambda = 2V/3 = 2\tilde{t}^2/3E_T$. Because of the non-local spin density involved in the interaction, the corresponding bare susceptibilities $\chi_{s\tilde{s}}^{(0)} = \chi_{\tilde{s}s}^{(0)}$ and $\chi_{\tilde{s}\tilde{s}}^{(0)}$ are also employed. They are obtained by multiplying the summed terms in Eq. (5·3) by a factor of $F_{\boldsymbol{k}+\boldsymbol{q},\boldsymbol{k}}$ (for $\chi_{s\tilde{s}}^{(0)}$) or $F_{\boldsymbol{k}+\boldsymbol{q},\boldsymbol{k}}^2$ (for $\chi_{\tilde{s}\tilde{s}}^{(0)}$). The resulting spin susceptibility reads

$$\chi_{ss} = \frac{\chi_{ss}^{(0)}}{D} \ , \quad D = \left(1 - \Lambda\chi_{\tilde{s}s}^{(0)}\right)^2 - \Lambda^2\chi_{ss}^{(0)}\chi_{\tilde{s}\tilde{s}}^{(0)} \ . \tag{5·5}$$

The no-double-occupancy constraint imposed on $H_{t\text{-}P}$ handled on a Gutzwiller level leads to a rescaling $\bar{\xi} = g_t\xi$ and $\bar{V} = g_P V$. Since the interaction term comes from the hopping, the Gutzwiller factors are equal $g_t = g_P \approx n_d$ and may be partially canceled in terms such as $\Lambda\chi^{(0)}$ leaving us with an effectively rescaled ω and T.

In Fig. 14 we show a sample result at the relative fraction of Co^{3+} ions $n_d = 0.5$. The bare spin susceptibility [Fig. 14(a)] is concentrated around the Γ point. When the interaction is switched on [Fig. 14(b)], the $2k_F$ ring in the susceptibility is enhanced. This suggests the fermionic $2k_F$-instabilities in a *Fermi-liquid* phase, consistent with a picture inferred from the experiment.[46] Interestingly, the RPA-spin susceptibility at $n_d = 0.5$ is most enhanced near the M point, i.e. near the observed magnetic Bragg peak position,[10] rather than at K typical for the AF Heisenberg
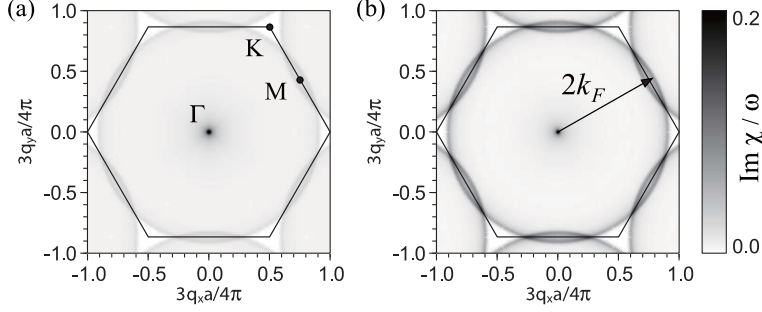
Fig. 14. (a) Map of bare χ_s''/ω for $n_d = 0.5$ (the average Co-valency 3.5) at $T = 0.025t$ and $\omega \to 0$. (b) Corresponding RPA-enhanced susceptibility calculated at $\tilde{t}^2/E_T = 3t$. The interaction enhances the susceptibility at the $2k_F$ ring which (at given density $n_d = 0.5$) nearly matches the Brillouin zone boundary. (After Ref. 30).)

spin system. In order to study the spin ordering at $n_d = 0.5$ more quantitatively, one should take into account also the Na ordering[7] which breaks a hexagonal symmetry of the underlying Fermi-surface.

The $2k_F$ antiferromagnetic correlations within our model are manifested in the temperature dependence of the nuclear spin relaxation rate $T_1^{-1} \sim (\sum_{\boldsymbol{q}} \operatorname{Im} \chi/\omega)_{\omega \to 0}$. According to the Korringa law, in the normal state $1/T_1 T$ should be temperature independent. This is the type of behavior experimentally observed in monolayer hydrate of $Na_x CoO_2$. However, in bilayer hydrates, which show a superconducting transition at T_c, $1/T_1 T$ is enhanced at low temperatures.[47],[48] This enhancement is stronger as T_c increases, eventually leading to a magnetic order.

We characterize the effect of the interaction (5·1) on $1/T_1 T$ by the enhancement factor $\langle F^2 \rangle$

$$\left(\frac{1}{T_1 T}\right)_{\mathrm{RPA}} = \langle F^2 \rangle \left(\frac{1}{T_1 T}\right)_{\mathrm{bare}}. \qquad (5\cdot6)$$

Using RPA enhanced χ_{ss} of Eq. (5·5) it can be approximately expressed as a double Fermi-surface average

$$\langle F^2 \rangle \approx \left\langle \frac{1}{D^2} \left[1 - \Lambda \operatorname{Re} \left(\chi_{s\tilde{s}}^{(0)} - F_{\boldsymbol{k},\boldsymbol{k}'} \chi_{ss}^{(0)} \right) \right]^2 \right\rangle_{\boldsymbol{k},\boldsymbol{k}' \in \mathrm{FS}}, \qquad (5\cdot7)$$

where $D(\boldsymbol{q}, \omega)$, $\chi_{s\tilde{s}}^{(0)}(\boldsymbol{q}, \omega)$ and $\chi_{ss}^{(0)}(\boldsymbol{q}, \omega)$ are evaluated at $\boldsymbol{q} = \boldsymbol{k}' - \boldsymbol{k}$, $\omega \to 0$.

The resulting enhancement factor at the relevant fraction of Co^{3+} $n_d \approx 0.5$ is presented in Fig. 15. To address the $T < T_c$ regime, we have included the approximate BCS gap $\Delta = 1.76 T_c \tanh(1.76\sqrt{T_c/T - 1})$ in our calculations. As the interaction strength Λ approaches its critical value for a magnetic ordering, the enhancement factor dramatically increases resembling the experimentally observed critical behavior.
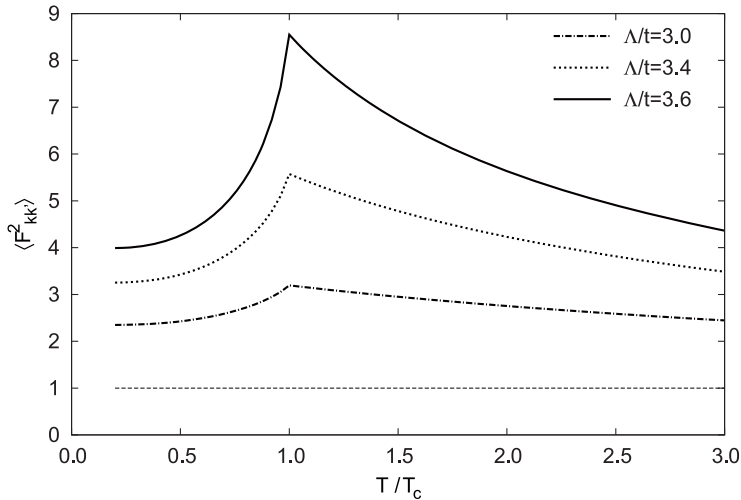
Fig. 15. Enhancement factor $\langle F^2 \rangle$ at $n_d = 0.5$, $t'/t = -0.2$ as a function of temperature. With the interaction switched off, $\langle F^2 \rangle = 1$. The interaction enhances $1/T_1 T$ near the superconducting transition temperature as the coupling constant increases. The critical coupling constant for a magnetic ordering in this case equals $\Lambda_{\mathrm{crit}} \approx 4t$.

§6. Superconductivity due to the pair-hopping interaction

Now, we consider the H_P Hamiltonian in the context of superconductivity. The kinetic energy coming from the pair-hopping interaction in H_P is optimized when Co^{4+} holes move pairwise. Eventually, this leads to their condensation into SC state. The difference from cuprates is that pairs are formed here not due to the superexchange (in cobaltates, J is small[49]) but because of the gain in the kinetic energy associated with $\tilde{t}$ hoppings. It is evident from Eqs. (4·1) and (4·2) that spin-singlet pairs gain much more kinetic energy than triplets. Alternatively, it can be said that the $S = 0$ Co^{3+} states move more coherently when the $S = 1/2$ background is in a singlet state. This result, explained in Fig. 11, is a consequence of quantum interference among the rich variety of spin states involved during the virtual process leading to Eq. (4·1).

A mean-field BCS analysis[*] of Eq. (4·1) shows that H_P supports either extended s-wave singlet SC with the gap function $\propto \gamma(\boldsymbol{k}) = \sqrt{2/3}(c_a + c_b + c_c)$, or doubly-degenerate spin-triplet p-wave pairing with $\gamma_{x,y}(\boldsymbol{k}) = \{(s_a - s_b), (2s_c - s_a - s_b)/\sqrt{3}\}$, where $s_\alpha = \sin k_\alpha$. The d-wave channel is repulsive, while the f-wave one is attractive but too weak in the physically reasonable doping range. We estimated the T_c from

$$ 1 = \sum_{|\bar{\xi}_{\boldsymbol{k}}| \leq E_T} \frac{\bar{V}_\alpha |\gamma_\alpha(\boldsymbol{k})|^2}{2\bar{\xi}_{\boldsymbol{k}}} \tanh \frac{\bar{\xi}_{\boldsymbol{k}}}{2T_c} \;, \tag{6.1} $$

where $\bar{V}_\alpha$ is either $\bar{V}$ or $\bar{V}/3$, and the corresponding formfactors are $\gamma(\boldsymbol{k})$ or $\gamma_{x,y}(\boldsymbol{k})$ for the singlet s-wave and triplet p-wave pairing, respectively. To account for

---

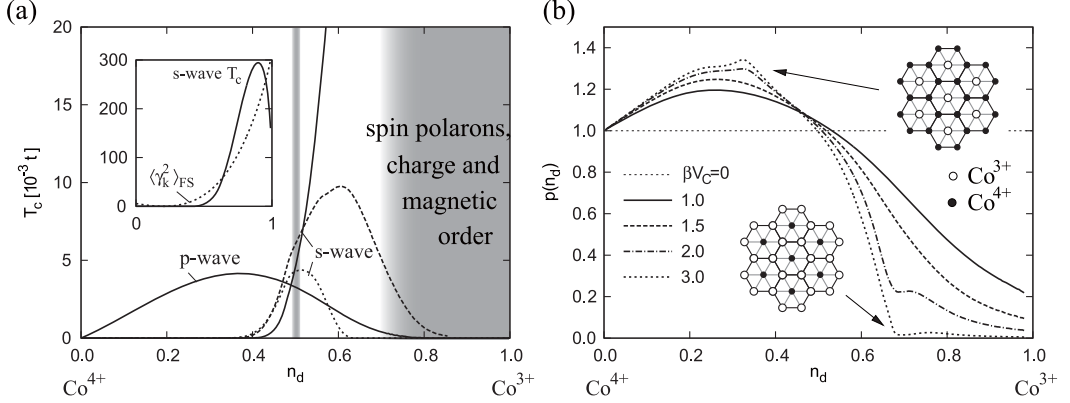[*] More details will be given in §7 in the context of the full orbital version of our model.

(a)

(b)

Fig. 16. (a) T_c in the extended s-wave and p-wave channels. The complete profile of the dominant, s-wave T_c curve is shown in the left inset together with $\gamma_{\boldsymbol{k}}^2$ (in arbitrary units) on the Fermi surface. The dashed ($\beta V_C = 1.5$) and dotted ($\beta V_C = 3$) T_c curves are calculated including nearest-neighbor Coulomb repulsion which reduces the pairing interaction V at large n_d. Shaded regions indicate the observed competing orderings (including the spin-charge order at $n_d = 0.5$). (b) Probability ratio $p(n_d)$ (see the text for its definition) renormalizing the pairing interaction at different values of nearest-neighbor Coulomb repulsion relative to the effective temperature $1/\beta \propto$ bandwidth. The feature at $n_d = 1/3$ for large V_C manifests a honeycomb-lattice formation where each Co^{3+} (○) has the maximum possible number of neighboring Co^{4+}-Co^{4+} pairs (●-●). Above $n_d = 2/3$, Co^{4+} holes can avoid each other completely if V_C is sufficiently large. (After Ref. 30).)

the no-double-occupancy constraint, the fermionic dispersion as well as the pair-hopping amplitude are renormalized by the Gutzwiller factor[37] $g_t = 2n_d/(1+n_d)$ as $(\bar{\xi}, \bar{V}) = (g_t\xi, g_t V)$, where n_d is the relative fraction of Co^{3+} ions. In the momentum summation, we have introduced a cutoff equal to the excitation energy E_T.

We solved Eq. (6·1) at $V = 3t$ (corresponding to $\tilde{t} = E_T = 3t$). In terms of the BCS-coupling constant, this translates into $\lambda = \bar{V}\bar{N} = VN \sim 1/3$ considering the density of states $N \sim 1/W \sim 1/9t$. Therefore, the present formulation in terms of an effective fermionic Hamiltonian (4·1) should give reasonable results. At larger values of V, we encounter a strong coupling regime where one should use the original model (2·2) instead and treat virtual spin states explicitly. This limit remains a challenging problem for future study.

The resulting T_c values from Eq. (6·1) are presented in Fig. 16(a) as solid lines. As expected, the highest T_c values are found in the singlet channel, increasing with Co^{3+} density due to the formfactor effect, until SC disappears at $n_d = 1$ limit. A weak triplet pairing is present thanks to its formfactor matching well the Fermi surface, but it is expected to be destroyed by (e.g. Na) disorder. (We should notice that these trends are based on the present mean-field decoupling which ignores collective spin fluctuations. One can speculate, for instance, that the triplet pairing may be supported by ferromagnetic fluctuations within the CoO_2 planes observed[9] at *large* n_d limit).

As the SC pairing considered here is due to the pair-hopping, Coulomb repulsion between the holes will oppose it. This is not a big trouble at high density of Co^{4+}

spins (as they cannot avoid themselves) but becomes a severe issue in a spin-diluted regime at large n_d, where Coulomb repulsion reduces the process described in Fig. 9 hence the amplitude V. Instead, the formation of spatially separated spin-polarons (Fig. 7) is favored, and competing orderings take over, such as an in-plane ferromagnetism induced by a residual interactions between spin-polarons.[39],[40] To include the effects related to the Coulomb repulsion in the Gutzwiller fashion, we use an additional multiplicative factor reflecting the suppression of the probability p_{ijk} of having the required Co_i^{3+}-Co_j^{4+}-Co_k^{4+} configuration. We have determined this probability using a classical Monte-Carlo simulation of hardcore particles with nearest-neighbor Coulomb repulsion V_C moving on a hexagonal lattice of 1024 sites. The simulations were performed at different "effective temperatures" $1/\beta$ imitating the kinetic energy (of the order of bandwidth) which competes with the Coulomb repulsion in the real system. Plotted in Fig. 16(b) is the probability ratio $p(n_d) = p_{ijk}(V_C)/p_{ijk}(V_C = 0)$ for several values of βV_C. The corresponding T_c curves calculated with $\bar{V} \to p(n_d)\bar{V}$ locate the SC-dome near the valence 3.4, in a remarkable correspondence with experiment.[27]–[29] (The reported Co-valences $\sim$3.4,[27] $\sim$3.3,[28] $\sim$3.46[29] optimal for SC translate into $n_d = 0.6, 0.7, 0.54$).

Finally, our t-$\tilde{t}$ model provides a clear hint on the role of water-intercalation needed for SC in Na_xCoO_2. Without water, a random Na-potential induces some amount of spin-polarons locally (the origin of "Curie-Weiss metal" behavior[7]) which suppress the pairing among the remaining fermions the usual way. Once this potential is screened-out by the water layers, an intrinsic ground state of CoO_2 planes as in Fig. 16 is revealed. (This interpretation of the water effect is consistent with the absence of superconductivity in the monolayer hydrate of Na_xCoO_2, where the water resides in the Na layers.) The remaining "enemy" of SC is the Coulomb repulsion which prevents the pairing of dilute Co^{4+} fermions and supports the formation of spin-polarons and magnetism instead.[39] More pronounced polaron physics (because of the presence of large $S = 1$ $\mathcal{T}$-exciton and narrow bandwidth) explains why T_c in cobaltates is low compared to cuprates. Another mechanism for the water effect is provided by the band-structure calculations[50] that indicate a substantial flattening of the a_{1g} band-top and a reduction of the band splitting when the water-layers are present. To study the former effect, we have included negative t' in our calculation. Due to the combined effect of better formfactor utilization in the s-wave channel and Fermi velocity reduction this enhances singlet pairing as demonstrated in Ref. 30).

§7. Full orbital structure of the interaction and the role of e_g' pockets

Local density approximation (LDA) bandstructure calculations on Na_xCoO_2 predict the existence of e_g' parts of the Fermi surface.[51],[52] According to some theoretical explanations of the pairing mechanism in Na_xCoO_2, these so-called e_g' pockets may even play a crucial role.[53]–[55] In the ARPES experiments, however, no e_g' pockets are observed in the Fermi surface, and the corresponding band of e_g' symmetry is well below the Fermi level in Na_xCoO_2 at the relevant dopings. The reasons for such a discrepancy between LDA predictions and ARPES experiments became a highly
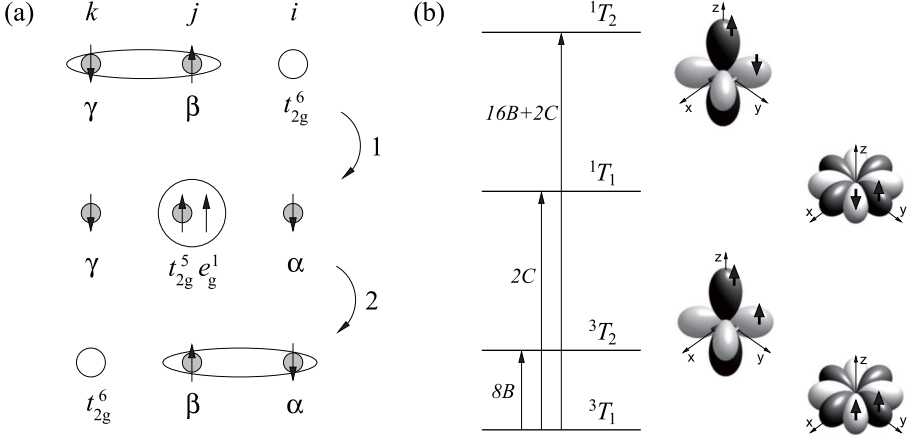
Fig. 17. (a) Virtual process leading to the effective interaction between the holes. Occupied t_{2g} hole orbitals are labeled by α, β, and γ respectively. The $\tilde{t}$-active orbitals α and γ are selected by the orientation of the $\langle ij \rangle$ and $\langle jk \rangle$ bonds. (b) Multiplet structure of a Co^{3+} ion in $t_{2g}^5 e_g^1$ configuration. Two lower triplet states $^3T_1$ and $^3T_2$ differ in the occupied e_g orbital being in-plane or out-of-plane with respect to the orbital occupied by the t_{2g} hole. B and C denote the Racah parameters.[56]

debated topic and are not yet fully understood.[32] Nevertheless, the e_g' band is reported to be located close to the Fermi level in the water-intercalated superconducting Na_xCoO_2,[13] which opens the question of its possible role in superconductivity.

The aim of this section is to investigate the implications of the proximity of e_g' states to the Fermi level within our model. To this end, we first derive a generalization of the effective interaction Hamiltonian (4·1) considering the full orbital structure of the initial, intermediate, and final states. Using such a generalized interaction Hamiltonian, we can study the case of mixed a_{1g}/e_g' topmost band to assess the effect of its e_g' parts. As the model bandstructure, we use the one from Ref. 37), where the multiorbital Gutzwiller approximation is applied to a tight-binding fit to LDA bands. The main advantage of this approach in the context of our study is the possibility to easily shift the position of e_g' band with respect to the Fermi level by tuning a single tight-binding parameter.

Instead of the projected a_{1g} holes we work here with the holes in canonical t_{2g} orbitals d_{xy}, d_{yz}, and d_{zx}. It is convenient to use the orbital angles introduced in Fig. 4(c) to specify the orbitals, e.g., $(\phi_a)_i$ annihilates a hole in d_{yz} orbital at site i. The a_{1g} hole operator f used in the previous sections corresponds to the linear combination $f_{j\sigma} = [(\phi_a)_{j\sigma} + (\phi_b)_{j\sigma} + (\phi_c)_{j\sigma}]/\sqrt{3}$ in the new notation.

To derive an effective Hamiltonian of the form (4·1), we consider the virtual process depicted in Fig. 17(a) which is an a_{1g}-unprojected equivalent of the process in Fig. 9. The initial state $|i\rangle$ of the two holes at sites k and j is either singlet $S_{kj}(\gamma\beta) = (\gamma_{k\uparrow}\beta_{j\downarrow} - \gamma_{k\downarrow}\beta_{j\uparrow})/\sqrt{2}$ or one of the triplet states $\boldsymbol{T}_{kj}(\gamma\beta) = \{\gamma_{k\uparrow}\beta_{j\uparrow}, (\gamma_{k\uparrow}\beta_{j\downarrow} + \gamma_{k\downarrow}\beta_{j\uparrow})/\sqrt{2}, \gamma_{k\downarrow}\beta_{j\downarrow}\}$. The t_{2g} orbitals γ and β of the two holes are now explicitly indicated. The γ orbital is the $\tilde{t}$-active t_{2g} orbital on $\langle jk \rangle$ bond. The amplitude of the transition to the final state $|f\rangle$ [either $S_{ij}(\alpha\beta)$ or one of

$\boldsymbol{T}_{ij}(\alpha\beta)$] contributing to the effective Hamiltonian $\mathcal{H}_P$ is evaluated as $\langle f|\mathcal{H}_P|i\rangle = -\sum_{\text{virt}}\langle f|\mathcal{H}_{\tilde{t}}|\text{virt}\rangle\langle\text{virt}|\mathcal{H}_{\tilde{t}}|i\rangle/E_{\text{virt}}$, where the summation runs over all possible intermediate states. These consist of a hole pair (α hole at site i and γ hole at site k) and the excited Co^{3+} ion at site j having the $t_{2g}^5 e_g^1$ configuration. The excitation energy depends on the spin and orbital combination of the t_{2g} hole and e_g electron of the Co^{3+} according to the multiplet structure presented in Fig. 17(b). The $\tilde{t}$-hopping Hamiltonian $\mathcal{H}_{\tilde{t}}$ used here provides the hopping between t_{2g} and e_g levels on nearest-neighbor Co ions as in Figs. 4(b) and (c). The resulting $\mathcal{H}_P$ Hamiltonian with full orbital structure can be written as

$$
\mathcal{H}_P = \sum_{\langle ijk\rangle}\sum_{\beta}\ \tilde{t}^2\Bigg[\cos(\alpha-\beta)\cos(\gamma-\beta)\left(\frac{3}{2}\frac{1}{E_{{}^3T_2}} - \frac{1}{2}\frac{1}{E_{{}^1T_2}}\right)
$$
$$
+ \sin(\alpha-\beta)\sin(\gamma-\beta)\left(\frac{3}{2}\frac{1}{E_{{}^3T_1}} - \frac{1}{2}\frac{1}{E_{{}^1T_1}}\right)\Bigg]\hat{S}_{ij}^{\dagger}(\alpha\beta)\hat{S}_{kj}(\gamma\beta)
$$
$$
+\tilde{t}^2\Bigg[\cos(\alpha-\beta)\cos(\gamma-\beta)\left(\frac{1}{2}\frac{1}{E_{{}^3T_2}} + \frac{1}{2}\frac{1}{E_{{}^1T_2}}\right)
$$
$$
+ \sin(\alpha-\beta)\sin(\gamma-\beta)\left(\frac{1}{2}\frac{1}{E_{{}^3T_1}} + \frac{1}{2}\frac{1}{E_{{}^1T_1}}\right)\Bigg]\hat{\boldsymbol{T}}_{ij}^{\dagger}(\alpha\beta)\hat{\boldsymbol{T}}_{kj}(\gamma\beta)\ ,
$$

$$(7\cdot1)$$

where α and γ are selected by the directions of the bonds $\langle ij\rangle$ and $\langle jk\rangle$ respectively. The cosine and sine factors come from the overlap of the $\tilde{t}$-active e_g orbitals at the respective bonds and the e_g orbitals participating in the virtual states. In the following, we neglect the contribution of the high-energy $S = 0$ states of Co^{3+}. The simpler version of the Hamiltonian in Eq. (7·1) as given by Eq. (4·1) is obtained by letting $E_{{}^3T_1} = E_{{}^3T_2} = E_T$ and projecting on the a_{1g} states.

Next we study the pairing interaction contained in (7·1). In §6, it was shown, that the singlet pairing channel leads to the SC dome similar to the experimentally observed one. We therefore concentrate on the singlet-hopping term in (7·1) and estimate T_c along the same lines as in §6. The corresponding singlet operators are first projected onto the topmost band (the closest to μ) $f_{\boldsymbol{k}\sigma} = u_{\boldsymbol{k}a}(\phi_a)_{\boldsymbol{k}\sigma}+u_{\boldsymbol{k}b}(\phi_b)_{\boldsymbol{k}\sigma}+u_{\boldsymbol{k}c}(\phi_c)_{\boldsymbol{k}\sigma}$ as the relevant one for a T_c estimation. A BCS Hamiltonian

$$
H_{\text{BCS}} = \sum_{\boldsymbol{k}\boldsymbol{k}'}V_{\boldsymbol{k}\boldsymbol{k}'}f_{\boldsymbol{k}\uparrow}^{\dagger}f_{-\boldsymbol{k}\downarrow}^{\dagger}f_{-\boldsymbol{k}'\downarrow}f_{\boldsymbol{k}'\uparrow}
\tag{7·2}
$$

is then extracted from the result. The formfactor $V_{\boldsymbol{k}\boldsymbol{k}'}$ has a complicated form containing the bandstructure coefficients $u_{\boldsymbol{k}\alpha}$ as well as the overlap factors in a triple sum over orbital angles

$$
V_{\boldsymbol{k}\boldsymbol{k}'} = 6\tilde{t}^2\sum_{\alpha\beta\gamma}(2-\delta_{\alpha\gamma})u_{\boldsymbol{k}\alpha}u_{\boldsymbol{k}\beta}u_{\boldsymbol{k}'\beta}u_{\boldsymbol{k}'\gamma}\cos k_{\alpha}\cos k_{\gamma}'
$$
$$
\times\left[\frac{1}{E_{{}^3T_1}}\sin(\alpha-\beta)\sin(\gamma-\beta) + \frac{1}{E_{{}^3T_2}}\cos(\alpha-\beta)\cos(\gamma-\beta)\right]\ .\tag{7·3}
$$

Table I. Character table for the C_{6v} group and a basis of its irreducible representations derived from $\cos k_\alpha$, $\sin k_\alpha$. These functions are orthonormal on the BZ, i.e., $\sum_{\bm{k}} \gamma_i(\bm{k})\gamma_j(\bm{k}) = \delta_{ij}$.

representation	E	$2C_6$	$2C_3$	C_2	$3\sigma_v$	$3\sigma_d$	function
A_1	1	1	1	1	1	1	$\gamma_s(\bm{k}) = \sqrt{\frac{2}{3}}\,(\cos k_a + \cos k_b + \cos k_c)$
B_1	1	-1	1	-1	1	-1	$\gamma_f(\bm{k}) = \sqrt{\frac{2}{3}}\,(\sin k_a + \sin k_b + \sin k_c)$
E_1	2	1	-1	-2	0	0	$\gamma_{p1}(\bm{k}) = \sin k_a - \sin k_b$
							$\gamma_{p2}(\bm{k}) = \frac{1}{\sqrt{3}}\,(2\sin k_c - \sin k_a - \sin k_b)$
E_2	2	-1	-1	2	0	0	$\gamma_{d1}(\bm{k}) = \cos k_a - \cos k_b$
							$\gamma_{d2}(\bm{k}) = \frac{1}{\sqrt{3}}\,(2\cos k_c - \cos k_a - \cos k_b)$

In principle, Eq. (7·3) in its present form can be used for the calculation of T_c, but to get a general insight to the results, a symmetry analysis of this formfactor is necessary. Guided by the group theory, we express Eq. (7·3) using symmetry-adapted functions.

In Table I, we show the irreducible representations of the C_{6v} group being the symmetry group of the hexagonal lattice of Co ions. The factors $\cos k_\alpha$ and $\cos k'_\gamma$ as well as the bandstructure coefficients u can be expressed in terms of functions belonging to A_1 and E_2 representation of the C_{6v} group (B_1 and E_1 is employed in the case of triplet pairing). The functions γ_s, γ_{d1}, and γ_{d2} allow us to directly express $\cos k_\alpha$ and $\cos k'_\gamma$, and the bandstructure coefficients u are converted to a symmetry-adapted form via the relations $a_{1g} = (u_a + u_b + u_c)/\sqrt{3}$, $e'_{g1} = (u_a - u_b)/\sqrt{2}$, $e'_{g2} = (2u_c - u_a - u_b)/\sqrt{6}$ deduced from Table I. We then perform the summations over α, β, and γ and regroup*) the resulting terms to form products of symmetric functions of $\bm{k}$ and $\bm{k}'$ respectively. For example, for the A_1 representation (corresponding to the extended s-wave symmetry) there exist four such functions $\Psi_{s1} = \gamma_s a_{1g} a_{1g}$, $\Psi_{s2} = \frac{1}{\sqrt{2}}\left(\gamma_{d1} a_{1g} e'_{g1} + \gamma_{d2} a_{1g} e'_{g2}\right)$, $\Psi_{s3} = \frac{1}{\sqrt{2}}\gamma_s \left(e'_{g1} e'_{g1} + e'_{g2} e'_{g2}\right)$, $\Psi_{s4} = \gamma_{d1}$, and $e'_{g1} e'_{g2} + \frac{1}{2}\gamma_{d2}(e'^2_{g1} - e'^2_{g2})$.

Disentangled interaction formfactor splits into the sum of s-wave, d_1-wave and d_2-wave contributions; i.e., these channels are independent in our BCS Hamiltonian. The formfactor of the s-wave channel reads as

$$V^{(s\text{-wave})}_{\bm{k}\bm{k}'} = \lambda \bm{\Psi}^T(\bm{k})(M_1 + r M_2)\bm{\Psi}(\bm{k}'), \qquad (7\cdot4)$$

where we have introduced the vector $\bm{\Psi}^T(\bm{k}) = [\Psi_{s1}(\bm{k}), \Psi_{s2}(\bm{k}), \Psi_{s3}(\bm{k}), \Psi_{s4}(\bm{k})]$, the coupling constant $\lambda = \tilde{t}^2/E_{3T_1}$, the ratio of the triplet excitation energies $r =$

---

*) This procedure is quite involved, since Eq. (7·3) at this stage contains a huge number of terms.
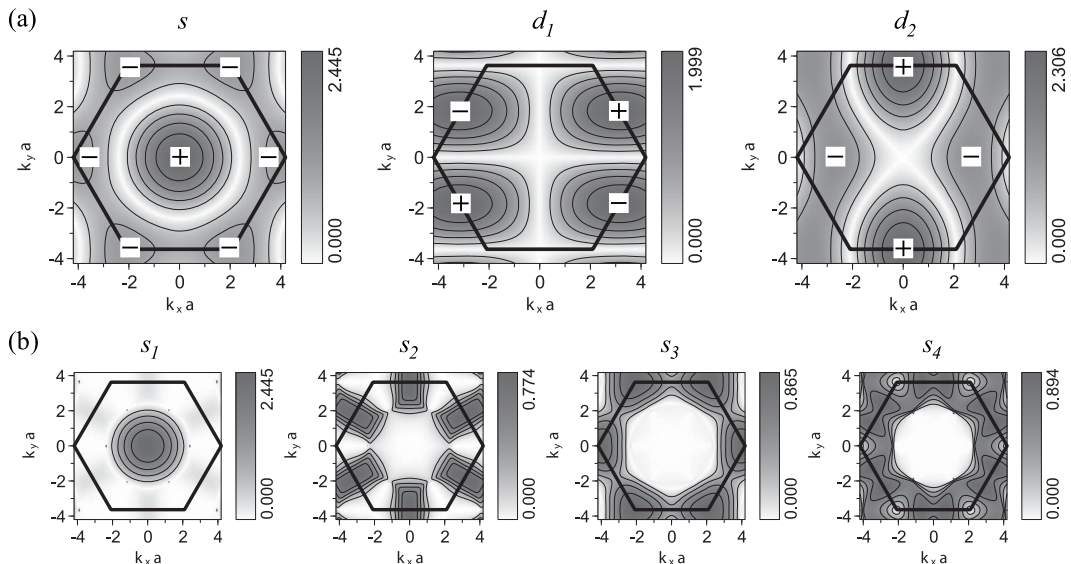
Fig. 18. (a) Symmetry functions $\gamma_s(\boldsymbol{k})$, $\gamma_{d1}(\boldsymbol{k})$ and $\gamma_{d2}(\boldsymbol{k})$ entering the singlet-channel BCS interaction (7·5) resulting from (7·1) in the simple a_{1g} case. (b) Symmetry adapted functions entering the BCS interaction in the singlet, extended s-wave channel in the general case. The bandstructure from Ref. 37) at $n_d = 0.5$ was used here.

E_{3T_1}/E_{3T_2} and the matrices

$$M_1 = \frac{1}{4}\begin{pmatrix} -2 & -\sqrt{2} & +\sqrt{2} & -\sqrt{2} \\ -\sqrt{2} & -1 & +1 & -1 \\ +\sqrt{2} & +1 & -1 & +1 \\ -\sqrt{2} & -1 & +1 & -1 \end{pmatrix}, \quad M_2 = \frac{1}{4}\begin{pmatrix} -2 & -3\sqrt{2} & -\sqrt{2} & +\sqrt{2} \\ -3\sqrt{2} & +1 & +7 & -7 \\ -\sqrt{2} & +7 & +9 & -9 \\ +\sqrt{2} & -7 & -9 & +9 \end{pmatrix}.$$

Each of the two d-wave channels could be represented in a similar way using 6×6 matrices and corresponding six symmetry adapted functions. It is instructive to see, how a simple a_{1g} expression emerges from the general result. In such case $a_{1g} = 1$ and $e'_{g1} = e'_{g2} = 0$ everywhere in the Brillouin zone implying $\Psi_{s1} = \gamma_s$, $\Psi_{s2} = \Psi_{s3} = \Psi_{s4} = 0$ and a similar reduction in the d-wave part. The simplified expression for the singlet-pairing formfactor could be written as

$$V_{\boldsymbol{k}\boldsymbol{k}'} = \frac{1+r}{2}\lambda\left[-\gamma_s(\boldsymbol{k})\gamma_s(\boldsymbol{k}') + 2\gamma_{d1}(\boldsymbol{k})\gamma_{d1}(\boldsymbol{k}') + 2\gamma_{d2}(\boldsymbol{k})\gamma_{d2}(\boldsymbol{k}')\right] \qquad (7\cdot5)$$

which shows an attractive extended s-wave part and a repulsive d-wave part. The symmetry functions γ_s, γ_{d1}, and γ_{d2} are presented in Fig. 18 along with the functions Ψ_{s1}, Ψ_{s2}, Ψ_{s3}, and Ψ_{s4} for the bandstructure of Ref. 37).

Finally, we estimate T_c in the singlet, extended s-wave channel using the disentangled formfactor (7·4). Plugging in our form of $V_{\boldsymbol{k}\boldsymbol{k}'}$ into the gap equation at $T = T_c$, we find that the transition temperature T_c is determined by the condition of the largest eigenvalue of the 4×4 matrix

$$-g_t\lambda(M_1 + rM_2)\sum_{\boldsymbol{k}}\boldsymbol{\Psi}(\boldsymbol{k})\boldsymbol{\Psi}^T(\boldsymbol{k})\frac{\tanh(\bar{\xi}_{\boldsymbol{k}}/2T_c)}{2\bar{\xi}_{\boldsymbol{k}}}, \qquad (7\cdot6)$$
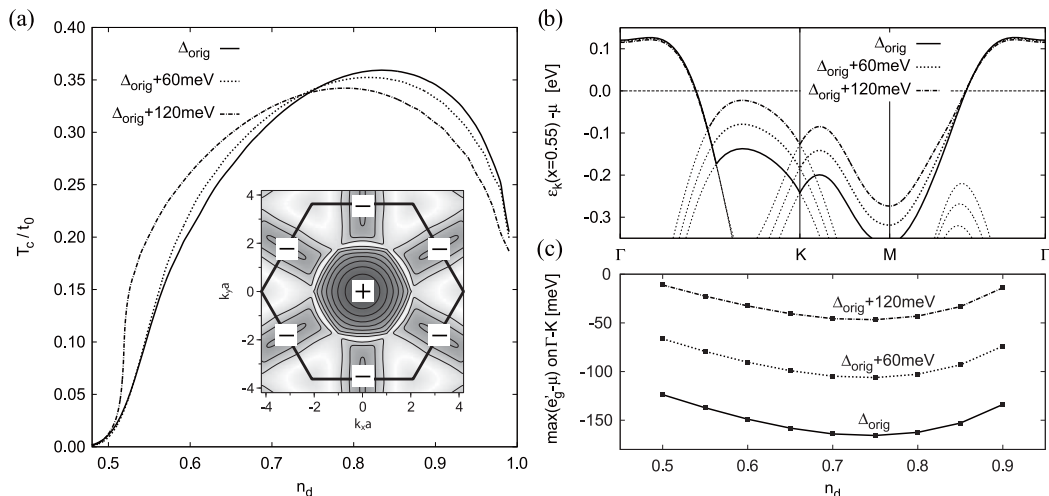
Fig. 19. (a) Transition temperature T_c as a function of n_d for the bandstructure of Ref. 37). The a_{1g}-e_g' orbital splitting Δ was modified to shift the e_g' bands closer to the Fermi level. $E_{3T_1} = \tilde{t}/2$, $r = 1/3$ was used in the calculation. The effect of the nearest-neighbor Coulomb repulsion is not included. The inset shows the gap function in the Brillouin zone. (b) The effect of the modified a_{1g}-e_g' orbital splitting on the bandstructure at $n_d = 0.55$. Topmost band employed in T_c calculation is drawn as a solid line. (c) Distance of the top of the e_g' band to the Fermi level as a function of n_d.

being equal to 1. Here $\bar{\xi}_{\boldsymbol{k}}$ is the dispersion of the renormalized topmost band.

Shown in Fig. 19 is the doping-dependent transition temperature as found from (7·6) employing the topmost band of the bandstructure of Ref. 37). To study the effect of the proximity of e_g' band to the Fermi level we have varied the a_{1g}-e_g' orbital splitting determining the position of the e_g' band. As observed in Fig. 19, T_c in the relevant range increases as the e_g' band approaches μ very closely, to around $10 - 30$ meV.

Another effect of the e_g' band is a strong anisotropy of the superconducting gap. In the pure a_{1g} case, the gap function as well as the nearest-neighbor tight-binding dispersion is proportional to $\gamma_s(\boldsymbol{k})$, so that the gap is totally isotropic at the Fermi surface. In the present case, the gap consists of the four symmetry functions presented in Fig. 18(b). Near the Brillouin zone center, where the topmost band is of a_{1g} character, the gap is again determined by $\gamma_s(\boldsymbol{k})$. However, closer to the Brillouin zone boundary, the band switches to mainly e_g' character and the functions Ψ_{s2}, Ψ_{s3} and Ψ_{s4} start to dominate the gap reversing its sign. They bring strong anisotropy to the gap function at the Fermi surface which attains $30 - 60\%$ at $n_d = 0.55$ depending on the a_{1g}-e_g' splitting. Such a strong anisotropy of the gap may lie behind the absence of the coherence peak in the nuclear spin relaxation rate data.[57],[58]

§8. Conclusions

We have discussed a strongly correlated model for $Na_x CoO_2$ which is based on the spin-state quasidegeneracy of $S = 0$ and $S = 1$ states of Co^{3+} and the specific

geometry of the CoO_2 planes in layered cobaltates. The basic idea of the model is that t_{2g}-e_g hopping of $3d$ electrons between nearest-neighbor cobalt ions, which is enabled thanks to the $90°$ geometry of Co-O-Co bonds, allows to employ the low-lying $S = 1$ $t_{2g}^5 e_g^1$ state of Co^{3+}. This new degree of freedom is exploited by the Co^{4+} holes as they move in the CoO_2 plane.

In the sodium-rich region, when the Co^{4+} holes are dilute, the model naturally explains experimentally observed strong correlations and interprets them in terms of a spin-polaron formation. At higher concentration of the doped holes, when the Fermi-liquid regime is established, we have derived effective interactions between the holes and discussed their impact on spin fluctuations. The superconductivity mediated by the spin-state fluctuations of Co^{3+} ions emerges in the model, at experimentally observed compositions. Finally, we discussed the symmetry of the effective interaction in the context of the possible role of e_g' bands in the superconductivity.

Given the simplicity and experimentally motivated design of the model, its success can hardly be accidental. Therefore, t-$\tilde{t}$ Hamiltonian, Eqs. (2·1) and (2·2), can be regarded as a basic minimal model for Na_xCoO_2. The idea of spin-state fluctuations may also have broader applications, e.g., in oxides of Rh and Ir ions with a similar spin-orbital structure and lattice geometry.

Formally, systems like $LaCoO_3$ and $NaCoO_2$ fall into the category of band insulators because Co^{3+} ions have an even number of electrons forming a completely filled, spinless configuration t_{2g}^6 in their ground state. Nevertheless, they are strongly correlated materials due to a proximity of virtual magnetic configurations of Co^{3+} which can easily be activated by doping, temperature, etc. We conclude that the presence of such low-lying magnetic states is responsible for the rich and nontrivial physics of cobaltates.

Acknowledgements

References

1) N. F. Mott, *Metal-Insulator Transitions* (Taylor and Francis, London, 1974).
2) I. Terasaki, Y. Sasago and K. Uchinokura, Phys. Rev. B **56** (1997), R12685.
3) Y. Wang, N. S. Rogado, R. J. Cava and N. P. Ong, Nature **423** (2003), 425.
4) M. Lee, L. Viciu, L. Li, Y. Wang, M. L. Foo, S. Watauchi, R. A. Pascal, R. J. Cava and N. P. Ong, Nature Materials **5** (2006), 537.
5) K. Takada, H. Sakurai, E. Takayama-Muromachi, F. Izumi, R. A. Dilanian and T. Sasaki, Nature **422** (2003), 53.
6) N. P. Ong and R. J. Cava, Science **305** (2004), 52.
7) M. L. Foo, Y. Wang, S. Watauchi, H. W. Zandbergen, T. He, R. J. Cava and N. P. Ong, Phys. Rev. Lett. **92** (2004), 247001.
8) C. Bernhard, A. V. Boris, N. N. Kovaleva, G. Khaliullin, A. V. Pimenov, Li Yu, D. P. Chen, C. T. Lin and B. Keimer, Phys. Rev. Lett. **93** (2004), 167003.
9) S. P. Bayrakci, I. Mirebeau, P. Bourges, Y. Sidis, M. Enderle, J. Mesot, D. P. Chen, C. T. Lin and B. Keimer, Phys. Rev. Lett. **94** (2005), 157205.
10) G. Gašparović, R. A. Ott, J.-H. Cho, F. C. Chou, Y. Chu, J. W. Lynn and Y. S. Lee, Phys. Rev. Lett. **96** (2006), 046403.

11) C. Bernhard, Ch. Niedermayer, A. Drew, G. Khaliullin, S. Bayrakci, J. Strempfer, R. K. Kremer, D. P. Chen, C. T. Lin and B. Keimer, Europhys. Lett. **80** (2007), 27005.

12) D. Qian, L. Wray, D. Hsieh, D. Wu, J. L. Luo, N. L. Wang, A. Kuprin, A. Fedorov, R. J. Cava, L. Viciu and M. Z. Hasan, Phys. Rev. Lett. **96** (2006), 046407.

13) T. Shimojima, K. Ishizaka, S. Tsuda, T. Kiss, T. Yokoya, A. Chainani, S. Shin, P. Badica, K. Yamada and K. Togano, Phys. Rev. Lett. **97** (2006), 267003.

14) D. Qian, L. Wray, D. Hsieh, L. Viciu, R. J. Cava, J. L. Luo, D. Wu, N. L. Wang and M. Z. Hasan, Phys. Rev. Lett. **97** (2006), 186405.

15) T. Valla, P. D. Johnson, Z. Yusof, B. Wells, Q. Li, S. M. Loureiro, R. J. Cava, M. Mikami, Y. Mori, M. Yoshimura and T. Sasaki, Nature **417** (2002), 627.

16) V. Brouet, A. Nicolaou, M. Zacchigna, A. Tejeda, L. Patthey, S. Hébert, W. Kobayashi, H. Muguerra and D. Grebille, Phys. Rev. B **76** (2007), 100403(R).

17) J. Bobroff, S. Hébert, G. Lang, P. Mendels, D. Pelloquin and A. Maignan, Phys. Rev. B **76** (2007), 100407(R).

18) C. de Vaulx, M.-H. Julien, C. Berthier, M. Horvatić, P. Bordet, V. Simonet, D. P. Chen and C. T. Lin, Phys. Rev. Lett. **95** (2005), 186405.

19) G. Lang, J. Bobroff, H. Alloul, P. Mendels, N. Blanchard and G. Collin, Phys. Rev. B **72** (2005), 094404.

20) C. de Vaulx, M.-H. Julien, C. Berthier, S. Hébert, V. Pralong and A. Maignan, Phys. Rev. Lett. **98** (2007), 246402.

21) D. Qian, L. Wray, D. Hsieh, L. Viciu, R. J. Cava, J. L. Luo, D. Wu, N. L. Wang and M. Z. Hasan, Phys. Rev. Lett. **97** (2006), 186405.

22) K. Takada, H. Sakurai, E. Takayama-Muromachi, F. Izumi, R. A. Dilanian and T. Sasaki, J. Solid State Chem. **177** (2004), 372.

23) M. L. Foo, R. E. Schaak, V. L. Miller, T. Klimczuk, N. S. Rogado, Y. Wang, G. C. Lau, C. Craley, H. W. Zandbergen, N. P. Ong and R. J. Cava, Solid State Commun. **127** (2003), 33.

24) R. E. Schaak, T. Klimczuk, M. L. Foo and R. J. Cava, Nature **424** (2003), 527.

25) P. W. Anderson, Science **235** (1987), 1196.

26) P. Fazekas and P. W. Anderson, Philos. Mag. **30** (1974), 423.

27) K. Takada, K. Fukuda, M. Osada, I. Nakai, F. Izumi, R.A. Dilanian, K. Kato, M. Takata, H. Sakurai, E. Takayama-Muromachid and T. Sasaki, J. Mater. Chem. **14** (2004), 1448.

28) C. J. Milne, D. N. Argyriou, A. Chemseddine, N. Aliouane, J. Veira, S. Landsgesell and D. Alber, Phys. Rev. Lett. **93** (2004), 247007.

29) M. Karppinen, I. Asako, T. Motohashi and H. Yamauchi, Chem. Mater. **16** (2004), 1693.

30) G. Khaliullin and J. Chaloupka, Phys. Rev. B **77** (2008), 104532.

31) J. Chaloupka and G. Khaliullin, Phys. Rev. Lett. **99** (2007), 256406.

32) D. Pillay, M. D. Johannes, I. I. Mazin and O. K. Andersen, arXiv:0804.3768.

33) S. Maekawa, T. Tohyama, S. E. Barnes, S. Ishihara, W. Koshibae and G. Khaliullin, *Physics of Transition Metal Oxides*, Springer Series in Solid State Sciences, vol. 144 (Springer-Verlag, Berlin, 2004).

34) M. W. Haverkort, Z. Hu, J. C. Cezar, T. Burnus, H. Hartmann, M. Reuther, C. Zobel, T. Lorenz, A. Tanaka, N. B. Brookes, H. H. Hsieh, H.-J. Lin, C. T. Chen and L. H. Tjeng, Phys. Rev. Lett. **97** (2006), 176405.

35) S. Yamaguchi, Y. Okimoto, H. Taniguchi and Y. Tokura, Phys. Rev. B **53** (1996), R2926.

36) A. Maignan, V. Caignaert, B. Raveau, D. Khomskii and G. Sawatzky, Phys. Rev. Lett. **93** (2004), 026401.

37) S. Zhou, M. Gao, H. Ding, P. A. Lee and Z. Wang, Phys. Rev. Lett. **94** (2005), 206401. They find the nearest-neighbor inter-orbital hopping $t' = -157.8$ meV. Projection to the a_{1g}-hole subband yields $t = -2t'/3 \simeq 0.1$ eV.

38) W. Koshibae and S. Maekawa, Phys. Rev. Lett. **91** (2003), 257003.

39) G. Khaliullin, Prog. Theor. Phys. Suppl. No. 160 (2005), 155.

40) M. Daghofer, P. Horsch and G. Khaliullin, Phys. Rev. Lett. **96** (2006), 216404.

41) M. Roger, D. J. P. Morris, D. A. Tennant, M. J. Gutmann, J. P. Goff, J.-U. Hoffmann, R. Feyerherm, E. Dudzik, D. Prabhakaran, A. T. Boothroyd, N. Shannon, B. Lake and P. P. Deen, Nature **445** (2007), 631.

42) See, e.g., C. L. Kane, P. A. Lee and N. Read, Phys. Rev. B **39** (1989), 6880.

43) J.-P. Rueff, M. Calandra, M. d'Astuto, Ph. Leininger, A. Shukla, A. Bosak, M. Krisch,

  H. Ishii, Y. Cai, P. Badica, T. Sasaki, K. Yamada and K. Togano, Phys. Rev. B **74** (2006), 020504(R).
44) A. S. Mishchenko and N. Nagaosa, Phys. Rev. Lett. **93** (2004), 036402.
  O. Rösch and O. Gunnarsson, Phys. Rev. Lett. **93** (2004), 237001.
45) C. A. Marianetti and G. Kotliar, Phys. Rev. Lett. **98** (2007), 176405.
46) J. Bobroff, G. Lang, H. Alloul, N. Blanchard and G. Collin, Phys. Rev. Lett. **96** (2006), 107201.
47) Y. Kobayashi, M. Yokoi and M. Sato, J. Phys. Soc. Jpn. **72** (2003), 2161.
48) Y. Ihara, H. Takeya, K. Ishida, H. Ikeda, C. Michioka, K. Yoshimura, K. Takada, T. Sasaki, H. Sakurai and E. Takayama-Muromachi, J. Phys. Soc. Jpn. **75** (2006), 124714.
49) See, e.g., Q.-H. Wang, D.-H. Lee and P. A. Lee, Phys. Rev. B **69** (2004), 092504.
50) M. D. Johannes and D. J. Singh, Phys. Rev. B **70** (2004), 014507.
51) D. J. Singh, Phys. Rev. B **61** (2000), 13397.
52) K.-W. Lee, J. Kuneš and W. E. Pickett, Phys. Rev. B **70** (2004), 045104.
53) M. D. Johannes, I. I. Mazin, D. J. Singh and D. A. Papaconstantopoulos, Phys. Rev. Lett. **93** (2004), 097005.
54) K. Kuroki, Y. Tanaka and R. Arita, Phys. Rev. Lett. **93** (2004), 077001.
55) M. Mochizuki, Y. Yanase and M. Ogata, Phys. Rev. Lett. **94** (2005), 147005.
56) J. S. Griffith, *The Theory of Transition Metal Ions* (Cambridge University Press, Cambridge, 1961).
57) T. Fujimoto, G. Zheng, Y. Kitaoka, R. L. Meng, J. Cmaidalka and C. W. Chu, Phys. Rev. Lett. **92** (2004), 047004.
58) K. Ishida, Y. Ihara, Y. Maeno, C. Michioka, M. Kato, K. Yoshimura, K. Takada, T. Sasaki, H. Sakurai and E. Takayama-Muromachi, J. Phys. Soc. Jpn. **72** (2003), 3041.